Carbon dioxide distribution, origins, and transport along a frontal boundary during summer in mid-latitudes

Arkayan Samaddar[1,1], Sha Feng[1], Thomas Lauvaux[2,2], Zachary Robert Barkley[1,1], Sandip Pal[3,3], Kenneth J. Davis[2,2], and Sha Feng[1]

[1]The Pennsylvania State University
[2]Pennsylvania State University
[3]Department of Geosciences, Atmospheric Science Division, Texas Tech University

November 30, 2022

Abstract

Synoptic weather systems are a major driver of spatial gradients in atmospheric CO2 mole fractions. During frontal passages air masses from different regions meet at the frontal boundary creating significant gradients in CO2 mole fractions. This study quantitatively describes the atmospheric transport of CO2 mole fractions during a mid-latitude cold front passage and explores the impact of various sources of CO2. We focus here on a cold front passage over Lincoln, Nebraska on August 4th, 2016 observed by aircraft during the Atmospheric Carbon and Transport (ACT)-America campaign. A band of air with elevated CO2 was located along the frontal boundary. Differences in CO2 across the front were as high as 25 ppm. Numerical simulations using WRF-Chem at cloud resolving resolutions (3km) coupled with CO2 surface fluxes and boundary conditions from CarbonTracker (CT-NRTv2017x) were performed to explore atmospheric transport at the front. Model results demonstrate that the frontal CO2 difference in the upper troposphere can be explained largely by inflow from outside of North America. This difference is modified in the atmospheric boundary layer and lower troposphere by continental surface fluxes, dominated in this case by biogenic and fossil fuel fluxes. Horizontal and vertical advection are found to be responsible for the distribution of CO2 mole fractions along the frontal boundary. This study highlights the use of high-resolution simulations in capturing CO2 transport along a frontal boundary.

Carbon dioxide distribution, origins, and transport along a frontal boundary during summer in mid-latitudes

Arkayan Samaddar[1], Sha Feng[1], Thomas Lauvaux[2], Zachary R. Barkley[1], Sandip Pal[3], Kenneth J. Davis[1,4]

[1]Department of Meteorology and Atmospheric Science, The Pennsylvania State University, University Park, PA 16802, USA.
[2]Laboratoire des Sciences du Climat et de l'Environnement, CEA, CNRS, UVSQ/IPSL, Universit Paris-Saclay, Orme des Merisiers, 91191 Gif-sur-Yvette CEDEX, France.
[3]Department of Geosciences, Mail Stop 1053, Texas Tech University, Lubbock, TX 79409, USA
[4]Earth and Environmental Systems Institute, The Pennsylvania State University, University Park, PA 16802, USA.

Key Points:

- High resolution simulation of a cold front passage captures the narrow band of elevated CO_2 ahead of the cold front.
- CO_2 inflow from the continental boundaries along with biogenic fluxes create the summertime frontal CO_2 distribution.
- Horizontal and vertical advection dominate atmospheric CO_2 transport along the frontal boundary.

Corresponding author: Arkayan Samaddar, `arkayan@psu.edu`

Abstract

Synoptic weather systems are a major driver of spatial gradients in atmospheric CO_2 mole fractions. During frontal passages, air masses from different regions meet at the frontal boundary creating significant gradients in CO_2 mole fractions. We quantitatively describe the atmospheric transport of CO_2 mole fractions during a mid-latitude cold front passage and explore the impact of various sources of CO_2. We focus here on a cold front passage over Lincoln, Nebraska on August 4th, 2016 observed by aircraft during the Atmospheric Carbon and Transport (ACT)-America campaign. A band of air with elevated CO_2 was located along the frontal boundary. Observed and simulated differences in CO_2 across the front were as high as 25 ppm. Numerical simulations using WRF-Chem at cloud resolving resolutions (3km), coupled with CO_2 surface fluxes and boundary conditions from CarbonTracker (CT-NRTv2017x), were performed to explore atmospheric transport at the front. Model results demonstrate that the frontal CO_2 difference in the upper troposphere can be explained largely by inflow from outside of North America. This difference is modified in the atmospheric boundary layer and lower troposphere by continental surface fluxes, dominated in this case by biogenic and fossil fuel fluxes. Horizontal and vertical advection are found to be responsible for the transport of CO_2 mole fractions along the frontal boundary. We show that cold front passages lead to large CO_2 transport events including a significant contribution from vertical advection, and that mid-continent frontal boundaries are formed from a complex mixture of CO_2 sources.

1 Introduction

Atmospheric CO_2 mole fractions have changed from 280 ppm during the pre-industrial period (circa. 1750) to present day mole fractions of 414 ppm (www.esrl.noaa.gov/gmd/ccgg/trends/). Over the last decade, the rate of increase in global atmospheric CO_2 mole fractions has risen from 1.8 ppm/year in 2008 to 2.4 ppm/year in 2018. These changes in atmospheric CO_2 have been linked to an increase in fossil fuel usage (Edenhofer et al., 2014; Skeie et al., 2011) and land use change (Houghton et al., 2012). About 55% of the CO_2 emissions are currently absorbed into oceans or terrestrial ecosystems (Le Quéré et al., 2018; Friedlingstein et al., 2019). In order to close the budget of atmospheric CO_2, the driving mechanisms of sources and sinks of CO_2 from continental surfaces and oceans need to be better quantified (Le Quéré et al., 2018). Studies have shown that northern hemisphere terrestrial ecosystems are a significant part of the terrestrial sink (Denning et al., 1995; Tans et al., 1990). However, uncertainties in estimates of global carbon sources and sinks exist due to lack of knowledge regarding primary drivers of the land sink (Huntzinger et al., 2017). Peylin et al. (2002) and Xiao et al. (2014) show that one of the key uncertainties in regional carbon flux estimates comes from errors in representation of atmospheric transport. Bastos et al. (2020) have investigated the sources of uncertainty in global scale models in the Global Carbon Budget (Le Quéré et al., 2018) and have found that among other factors, more in-situ observations help reduce uncertainties in atmospheric inversions.

Atmospheric transport models are used to determine sources and sinks of CO_2 through the process of inversion linking CO_2 mole fractions in the atmosphere to sources and sinks at the surface (Enting et al., 1995). In order for the inversion process to be accurate, these numerical transport models need to infer CO_2 sources and sinks with accuracy (Gurney et al., 2002). Evaluating the numerical models using CO_2 observation help determine the uncertainty in the ability of the models to reproduce the carbon cycle (H. W. Chen et al., 2019; Chevallier et al., 2019; Díaz-Isaac et al., 2018; Agustí-Panareda et al., 2019; Díaz Isaac et al., 2014).

Differences in the representation of transport processes within individual numerical models can lead to a biased representation of CO_2 (Schuh et al., 2019; Law et al., 1996; Houweling et al., 2010). Errors in the representation of boundary layer (ABL) dynamics (vertical mixing heights and horizontal wind profiles) in numerical models results in errors in inverse estimates of CO_2 (Lauvaux & Davis, 2014). Further studies evaluating both global and regional models also found that the simulated boundary layer depth in a numerical model has significant influence on the CO_2 distribution, and errors in the estimation of boundary layer depth is a major source of uncertainty in atmospheric transport representation (Geels et al., 2007). Synoptic scale weather events are an important part of atmospheric CO_2 transport and the representation of synoptic weather in numerical models is not addressed in studies focused on global scale and ABL evaluations.

The performance of regional and global models in capturing the synoptic scale variability of atmospheric CO_2 distribution has been evaluated (Law et al., 2008). Patra et al. (2008) and Sarrat et al. (2007) evaluated multiple global and regional scale numerical models and found that they were able to represent the observed synoptic scale CO_2 variability from tower and aircraft measurements. In order to improve the representation of atmospheric transport, the above studies suggest the use of higher horizontal and vertical resolution numerical models coupled with CO_2 fluxes with high temporal and spatial resolution (Agustí-Panareda et al., 2019; Geels et al., 2007). Numerical models running at global scale resolutions ($>$ 100s of km) represent mesoscale and microscale weather events through parameterizations of physical transport processes (Carvalho et al., 2014). A regional model study in east Asia has shown that numerical models running at higher resolutions than global models (27km horizontal grid resolution) were able to reproduce observed changes in atmospheric CO_2 mole fractions due to mesoscale weather systems (Ballav et al., 2012). The study also recommended the implementation of higher resolution transport models to better represent diurnal and synoptic variability of CO_2, as well as represent the changes in atmospheric CO_2 mole fractions by synoptic weather events.

Cold front passages are an example of synoptic scale events. Studies have shown that cold front passages have created gradients in atmospheric CO_2 mole fractions at the frontal boundary (Hurwitz et al., 2004; Lee et al., 2012). In Hurwitz et al. (2004), tall tower observations at Park Falls, Wisconsin, have studied four cold front passages over multiple seasons and shown that a summertime cold front passage resulted in changes in CO_2 mole fractions in the boundary layer. These changes were attributed to a pre-existing meridional gradient that was advected into the region as well as nearby biospheric fluxes. Horizontal advection and vertical mixing were hypothesized as the transport processes driving the changes in CO_2 mole fractions. Lee et al. (2012) reported that changes in CO_2 mole fractions caused by a cold front passage were greater than the gradients created due to typical diurnal variations on fair weather days. The changes in CO_2 mole fractions were dependent on the direction of cold front passage as well as the accumulation of CO_2 along the frontal boundary caused by wind shear and deformational flow. The ACT-America flight campaign provides a unique dataset of aircraft measurement across multiple cold fronts over continental United States. Continuous aircraft measurements across frontal boundaries captured the difference in CO_2 mole fractions between the warm and cold sectors for multiple frontal passages (Davis et al., 2018). For summertime cold fronts, a region of elevated CO_2 mole fractions was found along the frontal boundary (Pal et al., 2020). Mesoscale dynamics were seen to modulate the width and magnitude of the enhanced CO_2 region. These studies highlighted the significance, but did not quantify transport or simulate the processes leading to these structures.

The impact of synoptic scale events on atmospheric CO_2 mole fractions have also been simulated using various global and regional scale numerical models. Previous studies have shown that there is a correlation between atmospheric transport variables and biospheric CO_2 fluxes at synoptic scales resulting in large scale spatial gradients (Denning et al., 1995). Geels et al. (2004) found that the variability of CO_2 mole fractions in summer was highly correlated to the continental biospheric fluxes of CO_2 over the region. The horizontal transport of upstream features in CO_2 mole fractions also contribute significantly to the synoptic-scale CO_2 distribution. These interactions have been further explored in Chan et al. (2004), highlighting the response of simulated CO_2 mole fractions to changes in atmospheric conditions. Suppression of photosynthesis due to cloud cover ahead of the cold front resulted in increased CO_2 mole fractions. Cold front passage introduced air with elevated CO_2 mole fractions near the surface and vertical mixing in the warm sector was able to lift surface level CO_2 to the troposphere. Chan et al. (2004) also found that CO_2 gradients between 1 - 10 ppm/100km can be created by mesoscale horizontal and vertical transport processes within a day. In order to further understand the mechanisms driving the transport of atmospheric CO_2, a budget equation was developed (Bakwin et al., 2004). Using this equation on cold front passages showed that wind shear and deformational flow near the frontal boundary created strong CO_2 gradients that were advected horizontally along with the front (Parazoo et al., 2008). Studies have shown that for cold front passages, simulated CO_2 mole fractions are influenced by local surface fluxes along with horizontal and vertical transport processes over a timescale of a few days (Wang et al., 2007). Through these studies, it can be seen that the impact of cold front passages on the distribution of CO_2 is attributed to local fluxes of CO_2 interacting with upstream CO_2 gradients along the frontal boundary through horizontal and vertical transport.

Based on the recommendations from the previous studies investigating synoptic CO_2 variability, we use high-resolution WRF-Chem (Skamarock et al., 2008) simulation operating at 27km, 9km and 3km resolution. The resolution of 3km $\times$ 3km is capable of resolving some cloud convection (Klemp, 2006), presenting a more resolved description of frontal transport. We study a summer cold front passing over Lincoln, NE, USA using WRF-Chem v3.6.1. The transport of CO_2 is quantified using a budget equation identifying contributions from horizontal and vertical advection and vertical diffusion. Aircraft observations from the ACT-America campaign are used to evaluate the performance of the numerical results. Through this study we provide a unique cloud resolving resolution view of features in atmospheric CO_2 distribution during a single cold front passage. While past studies have highlighted the differences in CO_2 mole fractions between the warm and cold sectors, for this cold front passage, we show that along with the cross-sector difference, there is the presence of a narrow band of elevated CO_2 along the frontal boundary. We show that while biogenic sources and large scale inflow from the domain boundaries influence the cross-frontal difference in CO_2 mole fractions, the narrow band of elevated CO_2 was primarily driven by biogenic sources. Using a CO_2 budget equation (Parazoo et al., 2008; Bakwin et al., 2004), we highlight the interaction of horizontal advection, vertical advection, and vertical diffusion with CO_2 mole fractions during the cold front passage.

The current study is structured as follows the data and methods section describe the numerical model and the tools and analysis methods used for the current study. The results section characterizes the capabilities of the numerical modeling system and describes the CO_2 distribution along the frontal boundary and its evolution with time. Transport of CO_2 is broken out by terms in the conservation equation, including the impact of model grid-resolution on the representation of CO_2 transport. The final section highlights the implications of the current study for the broader scientific community.

2 Data and Numerical Framework

2.1 ACT-America Aircraft Measurements

The Atmospheric Carbon and Transport (ACT)-America mission is a NASA Earth Venture Suborbital mission designed to improve atmospheric inverse estimates of Greenhouse Gas (GHG) fluxes. One objective is to quantify and reduce atmospheric GHG transport uncertainties (Davis et al., 2020). Two aircraft, a NASA Wallops C-130 Hercules and a NASA Langley B200 King Air, collected remote and in-situ measurements in the boundary layer and free troposphere. During frontal passages, flight paths were designed to make measurements in both the warm and cold sectors by crossing frontal systems at multiple levels. Multiple vertical profiles were also collected on both sides of the front. In situ CO_2 measurements from the B200 and C-130 aircraft were collected using a PICARRO 2401-m spectrometer (Digangi et al., 2018) along with atmospheric state variables. Data sets are described by Davis et al. (2018). In the current study, we evaluated the performance of the numerical model using in-situ measurements from the ACT-America aircraft on August 4th, 2016.

2.2 Cold front passage on August 4th, 2016

The summer 2016 flight campaign was in the Midwest region of the U.S. from August 1st to August 17th. A cold front crossed south-eastern Nebraska, Iowa and northern Kansas (located within the 3km simulation domain) from August 4th 18Z to August 6th 09Z. Figure 1 shows the synoptic map for the frontal passage with the flight track overlay. The low-pressure center of the front was located over Manitoba in Canada. The cold front passage was characterized by a 170^o change in wind directions at the frontal boundary - northerly winds to southerly winds. The Lincoln airport station (KLNK) recorded that the daytime mean temperature dropped by 12 K between the 4th and 5th of August. The change in the air mass over the station was also accompanied by a 10% decrease in relative humidity and a 10 hPa drop in surface pressure. To capture the gradients in CO_2 mole fractions across the frontal boundary, the aircraft crossed the front at multiple altitudes (300 m, 3 km, 5 km and 8 km MSL) on August 4th between 16Z and 21Z. Vertical profiles were also taken at multiple locations in the warm and cold sector. The aircraft recorded a 25 ppm change in CO_2 (over a horizontal span of 40km) while crossing the frontal boundary in the atmospheric boundary layer (ABL) (Pal et al., 2020). Smaller cross-frontal mole fraction differences of the same sign were observed in the free troposphere (Pal et al., 2020).

2.3 Model Description

For the current study, we used the Weather Research and Forecasting Model with Chemistry - WRF-Chem ver. 3.6.1 (Skamarock et al., 2008). We ran the model with one-way nesting via three nested domains with spatial grid resolutions of 27 km, 9 km, and 3 km respectively, using WRF-Chem with a modification to include CO_2 as a passive tracer (Lauvaux et al., 2012). Figure 2 shows the arrangement of the nested domains as used in WRF-Chem. Vertical grid resolution has been kept constant across the domains with 51 terrain-following eta levels from the surface to the top of the atmosphere (at 100hPa). The vertical grids are staggered with 29 levels forming a higher density grid under 2km AGL (above ground level), with greater spacing above. The first vertical level has an elevation of 8m above ground level.

The simulations were initialized with meteorological driver data from 6-hourly ERA-Interim (Dee et al., 2011) outputs with a reduced Gaussian grid with approximately uniform 79 km spacing for surface and other grid-point fields (Berrisford et al., 2011) and NCEP high-resolution ($0.083° \times 0.083°$) SST data. Model physics are summarized in Table 1. We output WRF-Chem hourly for the period from July to August 2016, in which the model was re-initialized every 5 days and with 12-hour meteorological spin-up.

2.4 CO_2 Simulations

WRF-Chem transport was coupled with CO_2 fluxes from the CarbonTracker Near Real Time v2017 (CT-NRT.v2017) (Peters et al., 2007), hereafter referred to as CT-NRT.v2017. CO_2 is simulated as a passive tracer in the current study similar to setups described in prior studies (Butler et al., 2020; Feng, Lauvaux, Keller, et al., 2019; Feng, Lauvaux, Davis, et al., 2019). CT-NRT.v2017 provided surface fluxes as well as lateral boundary condi-

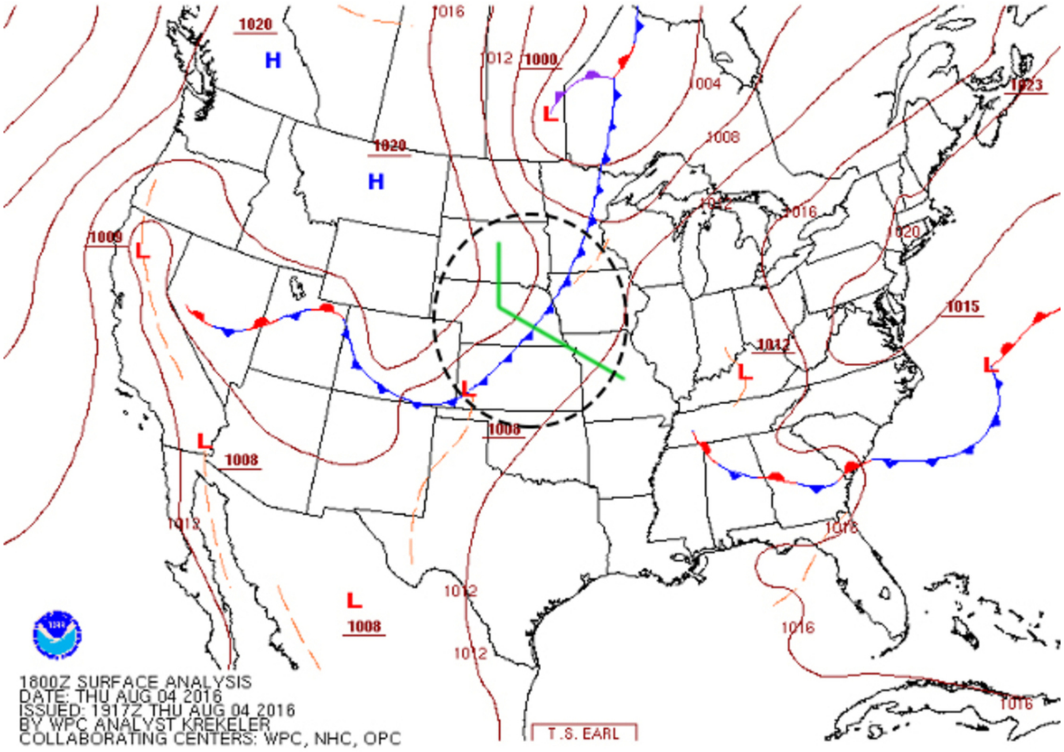

Figure 1. Synoptic map over continental U.S. on August 4th, 2016 at 18Z. The cold front studied is highlighted in the black dashed circle and the green line shows the approximate flight path for the ACT-America aircraft. Courtesy: NOAA/National Weather Service

Table 1. Parameterization options used for WRF-Chem simulations

Option	Parameter
Microphysics	Thompson (Thompson et al., 2008)
Boundary Layer Scheme	MYNN2 (Nakanishi & Niino, 2006)
Longwave Radiation	RRTMG longwave scheme (Iacono et al., 2008)
Shortwave Radiation	RRTMG shortwave scheme (Iacono et al., 2008)
Land Surface	Unified Noah land-surface model (F. Chen & Dudhia, 2001)
Cumulus Parameterization	Kain-Fritsch (new Eta) scheme (Kain, 2004), for the 27 km and 9 km resolution domains

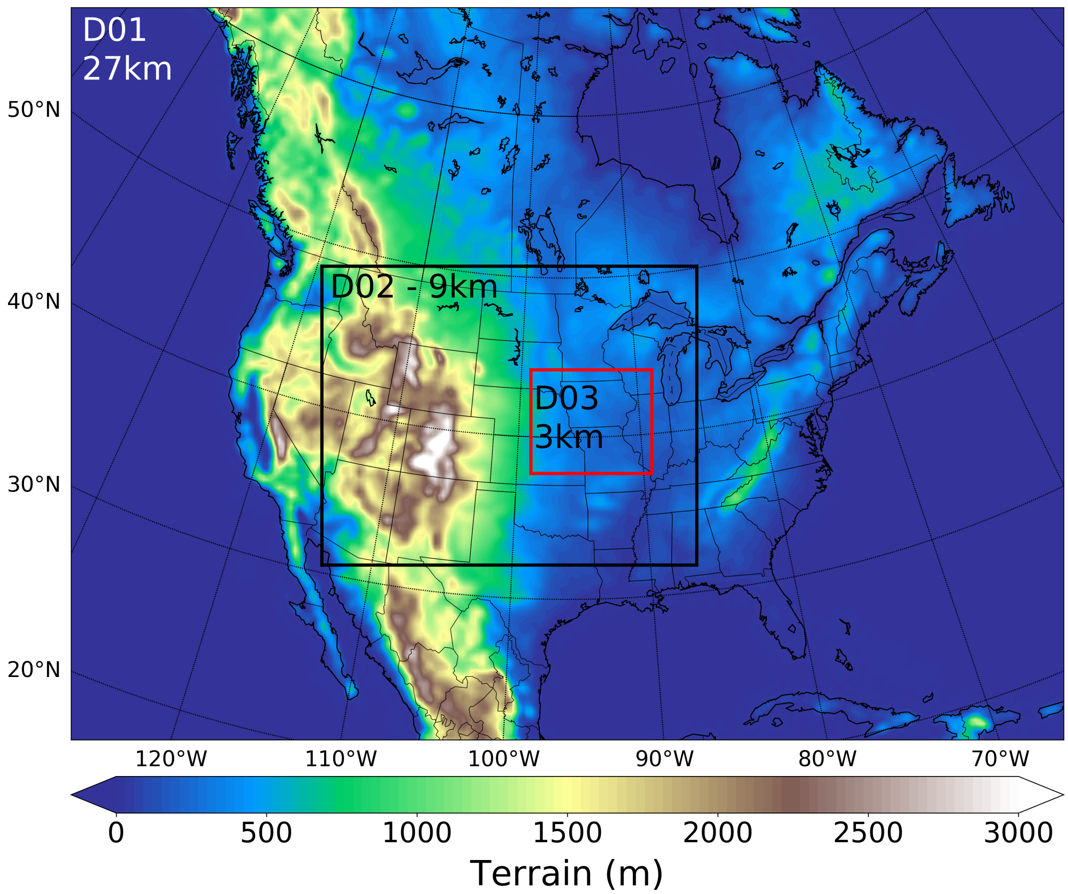

Figure 2. Domains used for the WRF-Chem model simulations, shown with contours of terrain height in meters above sea level. The map shows the 27 km resolution domain (D01), the black inner box shows the 9 km domain (D02) and the innermost red box shows the 3 km domain (D03).

tions. Within the WRF-Chem framework, these surface fluxes are tracked as individual tracers simulating fossil fuel emissions, biogenic fluxes, oceanic fluxes, and biomass burning emissions. CO_2 inflow from CT-NRT.v2017 to the boundaries of the WRF-Chem domains are tracked separately as lateral boundary condition tracers with the consideration of CO_2 mass conservation. Horizontal and vertical interpolations were applied using weights based on the pressure level differences between the two models. More details can be found in Butler et al. (2020). Thus, by considering the sum of all the individual tracers, the total atmospheric CO_2 mole fractions are determined. The lateral boundary conditions have a $3° \times 2°$ spatial resolution and the set of surface fluxes have a $1° \times 1°$ resolution over the study domain. Temporally, all the fluxes are introduced as 3-hourly mean values. The simulation is initialized with an atmosphere free of CO_2. Lateral boundary conditions along with surface fluxes populate the domain with CO_2 while WRF-Chem transport moves it within the domain. The regional model (WRF-Chem) simulation is initialized with an atmosphere devoid of any CO_2 mole fractions. Through surface emissions and inflow from the domain boundaries, CO_2 is introduced using information from Carbon Tracker NRT v2017. The high resolution WRF-Chem transport acts on these mole fractions to distribute CO_2 in the atmosphere. WRF-Chem was run for a month prior to the campaign period (July 2016) to ensure realistic CO_2 mole fractions (approximately 410 ppm) in the domain atmosphere before simulating the study period (August 2016).

2.5 Breakdown of CO_2 mole fractions into components

Within the WRF-Chem framework, the simulated atmospheric CO_2 mole fractions are calculated as the sum of components from CT-NRT.v2017, which are related to the various surface fluxes of CO_2 along with the lateral boundary conditions. By tracking the individual tracers, it is possible to show the interaction between atmospheric transport features created due to the cold front passage and CO_2 emitted from these various sources and the boundary conditions. In the current study, the CO_2 from the boundary conditions represent inflow from outside the simulation domains. These interactions can highlight which CO_2 tracer is impacted the most by the frontal passage. Further, a footprint analysis has also been performed to trace the origins of the air masses at the frontal boundary. Thus, by combining these two analyses it is possible to determine which sources of CO_2 were responsible for the atmospheric distribution during the period of frontal passage.

WRF-Chem was configured to simulate CO_2 originating from fossil fuel, biogenic, oceanic, and fire surface fluxes, and boundary conditions as separate tracers. Due to negligible impacts of oceanic and fire sources on CO_2 during the study period (< 1 ppm), we focus only on fossil fuel, biogenic and boundary condition tracers to investigate how the transport impacts them individually and quantify their contribution to specific features such as the band of elevated CO_2 mole fractions along the frontal boundary.

3 Methods

3.1 Model-Data Comparison

During the ACT-America flight campaign, CO_2 mole fractions along with standard atmospheric variables (potential temperature, water vapor mole fraction etc.) were measured on both aircraft (Davis et al., 2018). Similarly, simulated values of potential temperature and CO_2 mole fractions were extracted from WRF-Chem simulation atmosphere along the flight tracks to evaluate model performance. A limitation in this approach arose from the different time and spatial resolution of the products used. The modeled potential temperature and CO_2 mole fraction values were extracted from nearest points to the observations. The aircraft data are archived with a time resolution of 5 seconds (Davis et al., 2018), while the WRF-Chem setup used has been configured with hourly output.

For this evaluation, measurements taken within 30 minutes of a WRF-Chem output were used. In order to compare aircraft measurements along constant altitude flight legs, horizontal maps were extracted from WRF-Chem at the same altitude. A transect drawn almost parallel to the flight path was used to compare the vertical features of the front as described by WRF-Chem and the aircraft measurements.

3.2 Calculating CO_2 transport terms

As mentioned in section 2.4, CO_2 is simulated in WRF-Chem as a passive tracer. The transport of CO_2 is driven by the simulated atmospheric dynamics. Previous studies (Bakwin et al., 2004; Parazoo et al., 2008) have used the scalar conservation equation:

$$\underbrace{\frac{\partial C}{\partial t}}_{i} + \underbrace{\frac{RT}{p}\frac{F_c}{z_1}}_{ii} + \underbrace{K_m \frac{\partial^2 C}{\partial z^2}}_{iii} + \underbrace{w\frac{\partial c}{\partial z}}_{iv} + \underbrace{\overrightarrow{V_H} \cdot \nabla_H C}_{v} + \underbrace{g\frac{M\partial C}{\partial p}}_{vi} = 0 \tag{1}$$

to quantify CO_2 transport in the atmosphere where C is the CO_2 mole fractions in ppm, F_c is the surface flux of CO_2, z_1 is the lowest model level, R is the gas constant, T is temperature, p is pressure, K_m is the vertical eddy diffusivity coefficient, w is vertical velocity, $\overrightarrow{V_H}$ is horizontal velocity, g is gravity and M is the parameterized convective mass transport.

The individual terms represent the tendency in CO_2 mole fractions (i), influence of surface fluxes (ii), and transport by vertical diffusion (iii), vertical advection (iv), horizontal advection (v), and cloud convection (vi).

Term (ii) acts only on the lowest model layer. The cloud convective transport term is suitable for a model with parameterized convection. In the 3-km simulation, the convective transport is not separable from the grid-scale vertical advection and thus, in eq. 2, the new term (iv-modified) includes the vertical transport due to convection (vi) and vertical advection (iv) in eq. 1. We use lower-case c to indicate the differences. We continue to refer to term (iv-modified) as vertical advection for simplicity. Thus, at elevated model level (above the first level), the equation for cloud resolving resolution models can be further reduced to:

$$\underbrace{\frac{\partial C}{\partial t}}_{i} + \underbrace{K_m \frac{\partial^2 C}{\partial z^2}}_{iii} + \underbrace{w\frac{\partial c}{\partial z}}_{iv-modified} + \underbrace{\overrightarrow{V_H} \cdot \nabla_H C}_{v} = 0 \tag{2}$$

In our study, we showcase horizontal advection, vertical advection and vertical diffusion as the transport terms representing change in CO_2 mole fractions in the atmosphere. We study the impact of these terms on the distribution of CO_2 along a frontal boundary. Terms from eq. (2) were calculated using 3D velocities, CO_2 mole fractions and eddy diffusivity from WRF-Chem hourly outputs.

4 Results

4.1 Comparison to ACT-America Aircraft Measurements

WRF-Chem simulated a cold front with thermal features that are consistent with the aircraft measurements. Figure 3 shows the horizontal map and vertical cross-section of potential temperature from WRF-Chem and aircraft measurements. In figure 3(a) it can be seen that there is a region of warm air located in the south-west of the domain and a cold air mass to the north-west of the domain. Figure 3(b) shows the variability

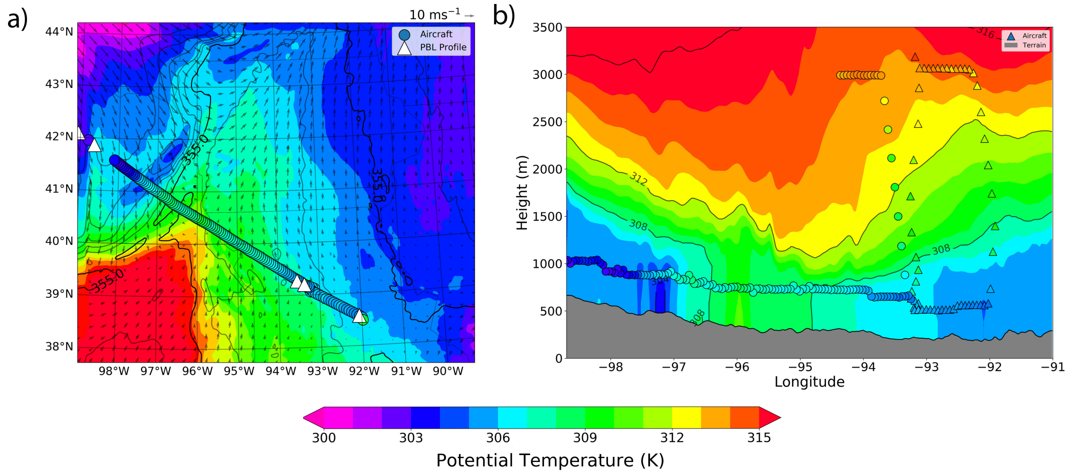

Figure 3. Comparisons of aircraft measurements to the high-resolution (3km) WRF-Chem simulation (at 548 m AGL) of potential temperature on August 4th, 2016 at 18Z. The aircraft measurements are shown as circles. Panel (a) shows simulated potential temperature overlaid with aircraft observations from approximately the same altitude, and (b) shows the vertical cross-section across the frontal boundary along the path traced by the aircraft transects. To match times with WRF-Chem outputs, aircraft measurements within ± 30 minutes of 18Z are shown. The white triangles in panel (a) show the location of vertical profiles used to calculate boundary layer depth.

in potential temperature in a vertical cross-section across the frontal boundary. The warm and cold air masses meet at -97° longitude at the surface. The vertical distribution of potential temperature shows that there is a band of warm air ($\theta > 307K$) extending from -97° to -94° longitude. This warm air mass was also present in the aircraft measurements.

Similar to potential temperature, WRF-Chem simulated wind speed and wind direction across the front that are largely consistent with the ACT-America aircraft observations. Figure 4(a) shows that in the ABL along the frontal boundary there is a decrease in wind speed at the frontal boundary as seen in the aircraft measurements and WRF-Chem; the feature is most prominent between -97° and -96° longitude and 40° and 41° latitude. In the cold sector, towards the northwest region of the domain, the higher wind speeds (>9 ms^{-1}) measured by the aircraft were also captured by WRF-Chem. Southerly winds in the warm sector have lower wind speeds (<9 ms^{-1}) in WRF-Chem as well as the aircraft measurements. WRF-Chem simulated wind speeds were found to be higher than the aircraft observations. Figure 4(b) shows that the simulated wind shift from northwesterly winds in the cold sector to southerly winds in the warm sector at the frontal boundary matches the wind shift measured by the aircraft. In the south-eastern end of the flight track, there is a region of relatively calm winds (<2 ms^{-1}) where there is a mismatch in wind direction between model and observations. However, this region is relatively far from the frontal boundary, and wind speeds are low in both the model and the observations.

Figure 3 shows the locations of the aircraft vertical profiles along the flight track where observed virtual potential temperature profiles were used to derive ABL depth and compare to the WRF-Chem diagnosed ABL depth. The WRF-Chem ABL depth was higher in the warm sector and lower in the cold sector. Table 2 summarizes the model-data differences between the warm and cold sectors. The cross-frontal difference was cal-

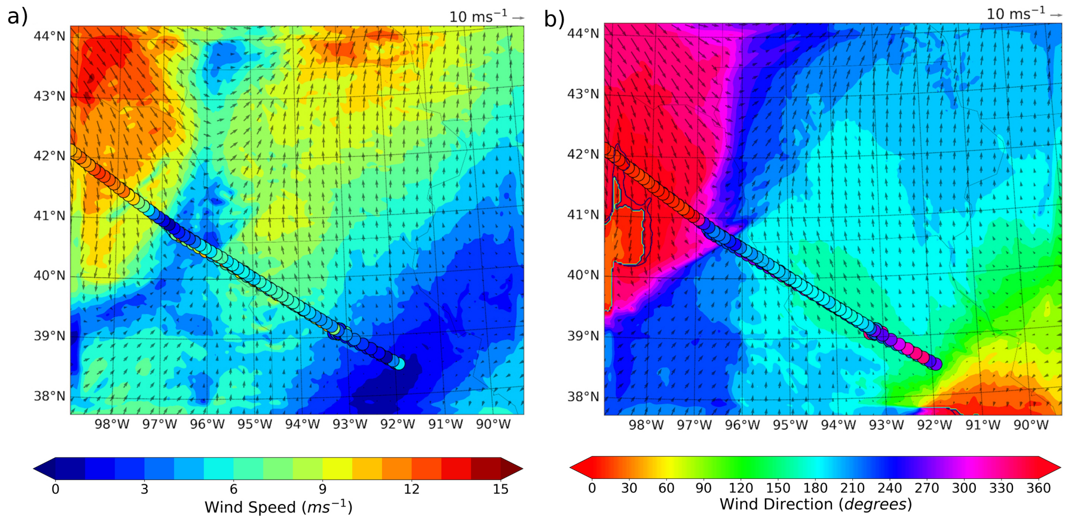

Figure 4. Comparisons of aircraft measurements to the high-resolution (3km) WRF-Chem simulation of horizontal winds on August 4th, 2016 at 18Z at an altitude of 548 m AGL. The aircraft measurements are shown as circles. Panel (a) shows the wind speed (ms-1) comparison with the WRF-Chem map overlaid with aircraft observations and panel (b) shows the wind direction (degrees) comparison with the WRF-Chem map overlaid with aircraft observations.

culated as a difference of the average values from the warm sector (between longitude -98° to -93° with southerly flow) and the cold sector (between longitude -99° to -96° with north-easterly flow) from WRF-Chem and the aircraft measurements. Studies conducted using similar WRF-Chem parameters have also reported values of the same order (Díaz-Isaac et al., 2018; Feng et al., 2016).

The response of simulated CO_2 mole fractions to the cold front over continental North America can be seen in Figure 5(a). The continental scale distribution of CO_2 shows large difference in warm-cold sector mole fraction (between 20-25 ppm) along the frontal boundary. In the cold sector, air with lower CO_2 mole-fractions ($<$ 390 ppm) are introduced with northwesterly winds coming in from Canada. The warm sector of the front is characterized with southerly flow bringing in air with higher CO_2 mole fractions (405-410 ppm). Figure 5(b), the high-resolution simulation, shows a zoomed-in view of the front and associated CO_2 distribution. An elongated band of air with higher CO_2 mole fractions can be seen extending along the frontal boundary. This band has a maximum width of approximately 200 km and extends from northeastern Kansas ($-99°$ longitude and 39° latitude)to northeastern Iowa ($-95°$ longitude and 44° latitude) spanning over 600 km. The white box delimits the boundaries of the innermost domain (Figure 5(a))

While simulated cross-frontal differences were as high as 25 ppm, observed frontal difference while similar in magnitude, were located northwest of the simulated boundary (between -98° to -97° longitude). WRF-Chem did simulate the lower CO_2 mole fractions observed in the cold sector north of 41° latitude. The horizontal extent of elevated CO_2 mole fractions in the warm sector is narrower in the model as compared to the aircraft measurements. This is specifically noticeable in figure 5(c) in WRF-Chem, the elevated concentrations extend from -96.5° to -94° longitude but in the aircraft measurements it extends from -97.7° to -93° longitude. This could be caused by a small error in the simulated location (Fig. 5(b)) of the high CO_2 region found in the model at approximately -95° longitude and 39° latitude.

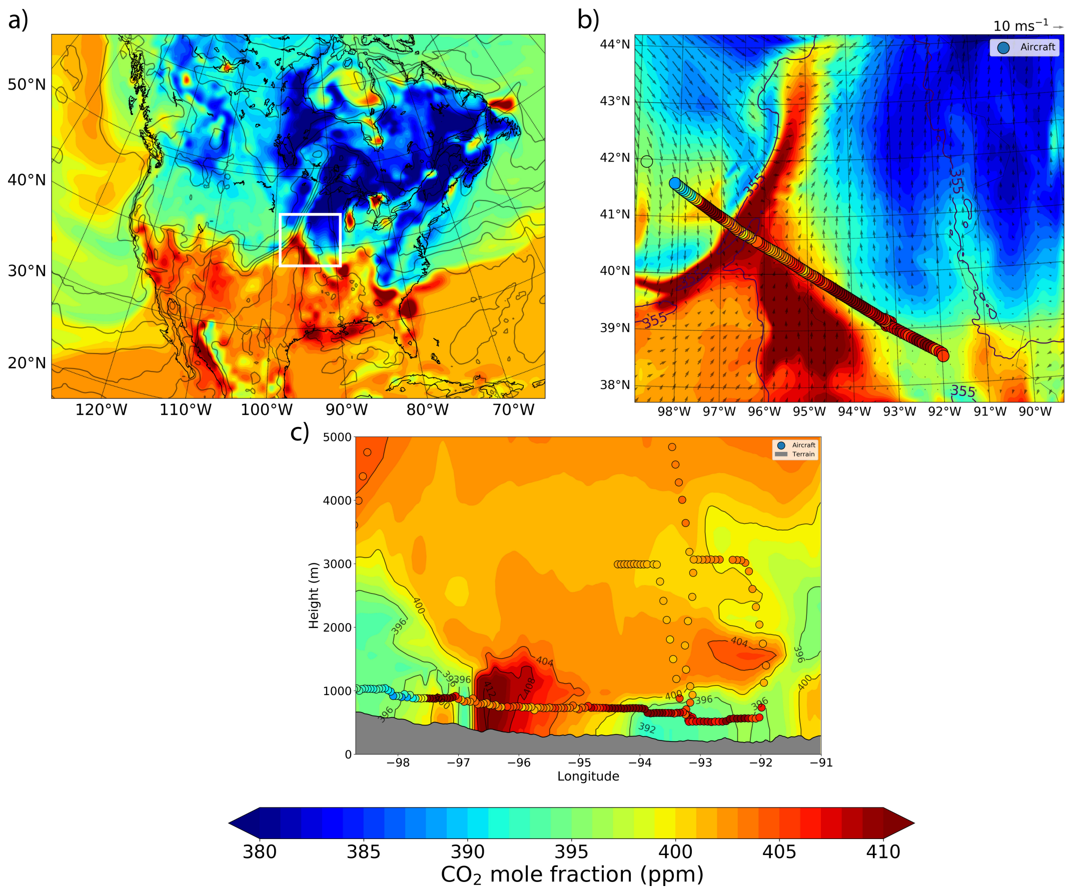

Figure 5. WRF-Chem simulated CO_2 mole fractions across continental U.S. and comparisons to aircraft measurements within the high-resolution (3km) domain on August 4th, 2016 at 18Z at an altitude of 548 m AGL. The aircraft measurements are shown as circles. Panel (a) shows the horizontal map of CO_2 mole fractions from the 27km domain highlighting the large scale features in CO_2 mole fraction, panel(b) shows simulated CO_2 mole fractions from the cloud resolving resolution 3km domain overlaid with aircraft observations. Panel (c) shows the vertical cross-section across the frontal boundary highlighting the vertical features as seen by WRF-Chem and the aircraft measurements.

Table 2. Evaluation of WRF-Chem using aircraft measurements in the boundary layer. Cross-frontal differences were calculated as the difference between warm sector and cold sector values

Variable	Units	Warm Sector		Cold Sector		Cross-Frontal Difference	
		WRF	Aircraft	WRF	Aircraft	WRF	Aircraft
Potential Temperature	K	313.2	311.7	305.4	307.2	7.8	4.5
Wind Speed	ms^{-1}	6.4	5.92	12.1	10.05	-5.7	-4.13
Wind Direction	degrees	242.9	259.96	310.75	308.71	-67.85	-48.75
ABL Depth	m AGL	836.4	770	692.6	705	143.8	65
CO_2 Mole Fraction	ppm	409.6	406.4	395.9	394.7	13.8	11.7

There is a small region of elevated CO_2 mole fractions west of the frontal boundary in the cold sector between -98° to -97° longitude. This was seen in both aircraft measurements and WRF-Chem. Overall, WRF-Chem was able to capture the large-scale features of the CO_2 distribution at frontal boundary, including the correct sign and approximate amplitude of the cross-frontal difference. Table 2 shows the quantified statistics comparing WRF-Chem and aircraft measurements along the flight track. The distribution of CO_2 in the simulated atmosphere is determined by interactions between atmospheric transport and the surface fluxes. The misalignment of the CO_2 distribution between WRF-Chem and aircraft can arise from errors either in transport or fluxes and detangling them to quantify the cause is beyond the scope of the current study. Based on the aircraft observations in figure 5(b), it can be seen that the observed frontal boundary was located 100 km to 120 km to the northeast of the simulated frontal boundary. Also, the southeastern part of the simulation domain has lower CO_2 mole fractions than the observations. the aircraft measurements were taken in the boundary layer. The region of mismatch in the southeastern (between $-93°$ and $-91°$ longitude) is likely a timing mismatch due to reduced wind speeds in the region ($\sim$ 0-2 ms^{-1}) as the elevated CO_2 mole fractions were not advected in time. On August 4th at 20Z, the simulated CO_2 mole fractions in the region between $-93°$ and $-92°$ longitude are closer to aircraft measured values ($<$ 2 ppm difference). The cold sector wind speeds were higher in WRF-Chem, in comparison to aircraft measurements by 2 ms^{-1} which can lead to the front moving faster in the simulation. In addition to the discrepancies in the wind field in the warm and cold sector, WRF-Chem also simulated a stagnant air mass in the eastern part of the domain between $-93°$ and $-89°$ longitude with low CO_2 ($<$ 390 ppm). The presence of this stagnant air mass was not confirmed using aircraft measurements due to the spatial extent of the flights. The stagnant air mass could also be a cause for the discrepancy in CO_2 mole fractions between aircraft measurements and WRF-Chem.

Even though the CO_2 distribution was not exactly represented as measured by the aircraft, WRF-Chems performance in simulating the large-scale CO_2 features during the frontal passage as well as meteorological variability allows it to qualify as a platform to study CO_2 transport.

4.2 Synoptic-scale weather and CO_2 distributions on August 4^{th}

In the current study, WRF-Chem simulation of CO_2 distributions during the cold front passage show the presence of a narrow band of elevated mole fractions aligned with frontal boundary.

Figure 6 shows the distribution of equivalent potential temperature (θ_e) within the innermost simulation domain at an elevation of 548m AGL at 18Z on August 4th. The frontal location was determined by the maximum gradient in θ_e in the innermost high-

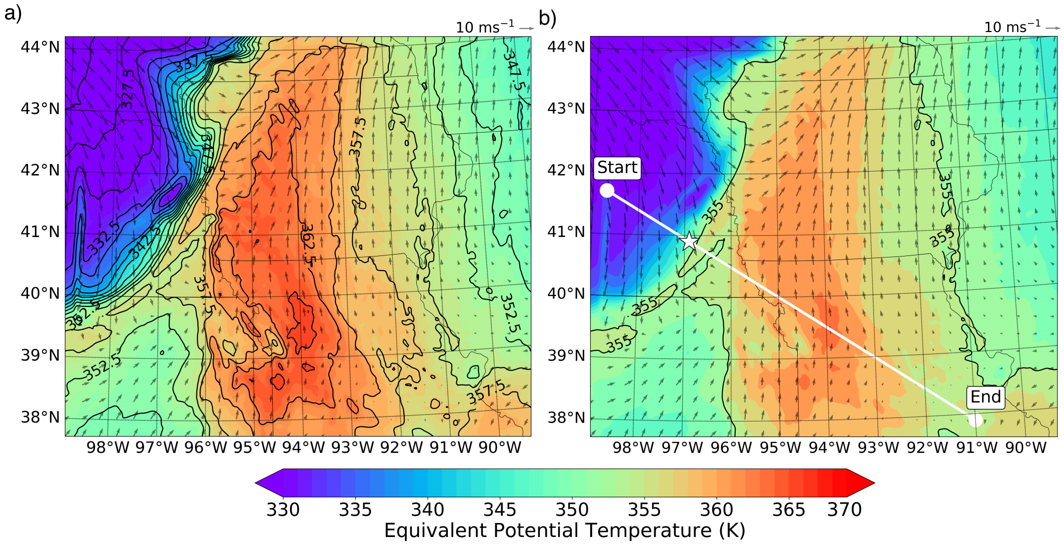

Figure 6. Map of equivalent potential temperature (θ_e) at an elevation of 548m (AGL) at 18Z on Aug 4th as simulated by WRF-Chem. Panel (a) shows the equivalent potential temperature distribution with contours used to determine the threshold value. Panel (b) shows the contour of equivalent potential temperature threshold value ($\theta_e = 355K$) highlighting the location of the front. The white line shows the transect used to study features across the frontal boundary in the warm and cold sector of the front. The star shows the location of the reference chosen for analysis in this study.

resolution domain (Pauluis et al., 2008). In figure 6(a), based on the contours of θ_e we can see that the cold front extends from the border of Minnesota and South Dakota (located at 44° longitude and -95° longitude) in the north to 40° latitude and -99° longitude at the western edge of the domain. The maximum gradient is located between -94° longitude and -97° longitude between the 41° latitude and 42° latitude. Based on the gradients in θ_e across the domain, we defined the frontal boundary as the contour line corresponding to a θ_e value of 355 K, which is highlighted in figure 6(b) as the single black contour line. In addition to θ_e, the locations of the warm and cold sectors of the front are further confirmed by the changing wind directions as seen in figures 6(a) and 6(b). The cold sector has predominantly north-westerly flow covering most of the northwestern region of the domain (between 40° to 44° north and -95° to -99° longitude), while the warm sector can be identified by warmer southerly winds between 37° to 45° north and -92° to -98° longitude.

We select the line extending across the front into the warm and cold sectors and a fixed-point location, referred hereafter as our reference location, where the frontal boundary passes at 18Z (see Figure 6b) to study the vertical structure of the atmospheric CO_2 and its evolution responding to this summertime cold front (Figure 7). Figure 7(a) shows the impact of the cold front passage on CO_2 contribution at a given time across the frontal boundary. In Figure 7(a), we see the slanted structure of the front in the cold sector (western region, lower altitudes) identified by air with much lower CO_2 mole fractions (380 395 ppm). The CO_2 distribution is largely correlated with the alignment of θ_e contours shown as the black contours. In comparison, the warm sector has elevated CO_2 mole fractions (-94° to -95° longitude) which extend from the surface to approximately 3.5 km MSL near the frontal boundary identified as the band of high CO_2 along the frontal boundary.

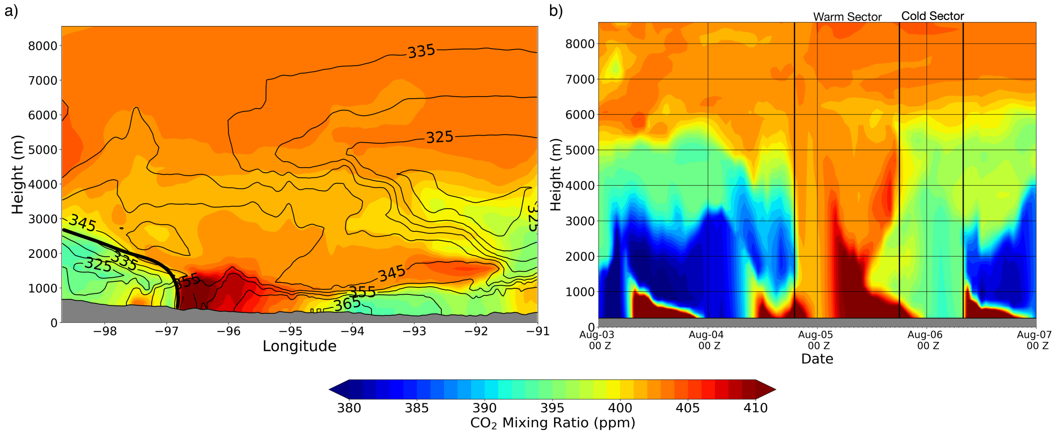

Figure 7. Vertical distribution of CO_2 during a cold front passage. (a) Vertical distribution (MSL) of CO_2 along the transect (white line in Figure 6b) shown in figure 6 highlighting the warm and cold sector of the front on August 4th at 18Z. The bold black line shows the slanted structure of the front in the cold sector with lower CO_2 mole fractions. (b) Time evolution of CO_2 mole fractions over the reference location (white star in Figure 6b at 40.9N and 96.9W) from Aug 3rd to Aug 7th 00Z. The gray regions show the terrain. The vertical black lines in panel (b) show the period of frontal influence from Aug 4th 18Z to Aug 6th 09Z over the reference location.The black vertical lines highlight the period of warm and cold sector passage over the location.

In order to track the influence of the cold front passage on local CO_2 distribution, a time-series of vertical distribution at the reference location is shown in figure 7(b). The location experiences elevated CO_2 mole fractions between August 4th at 18Z and August 5th at 18Z when the cold front crosses over the location introducing air mass with lower CO_2 mole fractions. The air mass with elevated CO_2 concentrations correspond to the warm sector of the front, lasting until Aug 5th 18Z. The warm sector air mass is followed by the cold sector air mass over the location with lower CO_2 mole fractions ($<$ 390ppm). This can be seen in figure 7(b) between Aug 6th 00Z and 09Z. The impact of the frontal passage over the location disrupts the repeated diurnal variation features (seen prior to Aug 4th 18Z). We also see that there are repeated patterns of high and low CO_2 mole fractions near the surface these are caused by the daily cycle of ecosystem fluxes and ABL mixing. Between 18Z Aug 4th and 18Z Aug 5th, when the warm sector air mass passes over the region, there is a period of elevated CO_2 mole fractions that is relatively uniform in the distribution, extending above 6km MSL. During this period, air mass with pre-existing gradients are being advected over the location - these gradients do not represent downward movement of air from higher up in the atmosphere. Beginning at Aug 5th 18Z, air mass above the reference location has low CO_2 mole fractions ($<$ 390ppm). This continues for a few more hours until Aug 6th 09Z when there is a sharp change (from 410 ppm to 392 ppm) in the vertical distribution of CO_2, showing the impact of the post-frontal air mass over the location. The Aug 6th 09Z change in the vertical distribution of CO_2 corresponds to the the pattern seen before the cold front entered the domain. The components of CO_2 as well as the transport mechanisms responsible for these features are described in greater detail in sections 4.3 and 4.4 respectively.

4.3 CO_2 transport from various sources

We find that CO_2 introduced into the domain via boundary conditions along with influences from biogenic and fossil fuel components within the domain determine the distribution of CO_2 along the frontal boundary. During this frontal passage, three distinct air masses were present over the region - (i) the cold sector air mass advected in from the northwest with low CO_2 mole fractions, (ii) the warm sector air mass with elevated CO_2 located in the southwestern region of the domain, and (iii) a stagnant air mass in the northeastern section of the domain with low CO_2 mole fractions. The stagnant air mass has high fossil fuel CO_2 mole fractions. However, strong negative biogenic signal results in low total CO_2 mole fractions. The cross-frontal difference (calculated near the surface at -97° longitude on August 4th at 18Z in figure 7(a)) in CO_2 mole fractions is similarly influenced by these components. Figure 8 shows the distribution and time-evolution of CO_2 mole fractions for each separate component from different perspectives. Based on the horizontal maps, at 18Z on Aug 4th, strong negative biogenic CO_2 (approximately -10 ppm) between -99° and -95° longitude and 40° and 44° latitude are co-located with the cold sector air mass with low CO_2 mole fractions as seen previously in figure 7(b). In the warm sector (between -96° and -94° longitude and 41° and 39° latitude), biogenic fluxes have strong positive magnitudes ($>$ 8ppm) and are aligned with air mass with elevated CO_2 mole fractions in figure 7(a). Additionally, along the frontal boundary there is a sharp change in biogenic CO_2 from -10 ppm to 10 ppm near the reference location (shown by the star in figure 8(a)). Figure 8(b) shows fossil fuel fluxes have elevated mole fraction in the eastern half (between -92° and -90° longitude) of the domain. The presence of stronger negative transported biogenic signal over the same region cancels out the impact of the elevated fossil fuel mole fractions. The frontal difference is visible in the horizontal map of boundary inflow CO_2. However the magnitude of the difference is lower (2-3 ppm) when compared to the total CO_2 distribution (20-25 ppm). Biogenic CO_2 shows a frontal difference of 20 ppm while the fossil fuel fluxes show a frontal difference of 4 ppm. These features are further discussed and differentiated by Pal et al. (2020).

Vertical features in the cross-frontal difference between CO_2 mole fractions is shown in figure 8 (panels (d) to (e)). The slanted vertical structure of the cold front seen in figure 7(a) is highly correlated with boundary condition CO_2 mole fractions. The cross-frontal CO_2 difference caused by boundary conditions was around 5 ppm near the surface. The boundary inflow does not modulate the elevated band of CO_2 along the frontal boundary. The narrow band of elevated CO_2 (2-6 ppm increase) is located near the frontal boundary from the surface extending to 2 km MSL, and between -97° and -96° longitude. This band of elevated CO_2, as well as the relatively lower ($\sim$ 392 ppm) near surface CO_2 mole fractions between -95° and -91° longitude are primarily influenced by biogenic CO_2 mole fractions due to the changes in biogenic CO_2. In figure 8(e), we see that fossil fuel has a positive contribution (2-4 ppm) near the frontal boundary (between -97° and -91° longitude), and that fossil CO_2 emissions are counteracted by the co-located strong biogenic CO_2 drawdown (-10 ppm) in the lower atmosphere - further confirming that the elevated CO_2 mole fractions from fossil fuel were not a major driver of frontal CO_2 anomalies during the Aug 4th cold front passage.

The time-evolution analysis of various components of CO_2 seen in figure 8, panels (g), (h) and (i), shows that during the period of frontal passage, there are changes in the near surface CO_2 mole fractions driven by biogenic sources, followed by fossil fuel sources acting on CO_2 advected in by boundary inflow. Variability in the vertical profile of biogenic CO_2 mole fractions are shown in figure 8(g). Diurnal net ecosystem exchange and deep ABL mixing can be seen as the repeating low CO_2 mole fractions extending into the lower troposphere, coupled with nocturnal respiration causing high CO_2 mole fractions near the surface. This pattern is disrupted on August 4th at 18Z, as elevated CO_2 mole fractions are present in the atmosphere above the reference location. The difference in near surface CO_2 mole fractions between the pre-frontal and frontal periods is 25 ppm as seen in figure 7(b). The elevated CO_2 mole fractions persist over the region for 30 hours followed by a shorter period of depleted CO_2 mole fractions. The diurnal pattern resumes around 09Z on August 6th. This disruption to the diurnal pat-

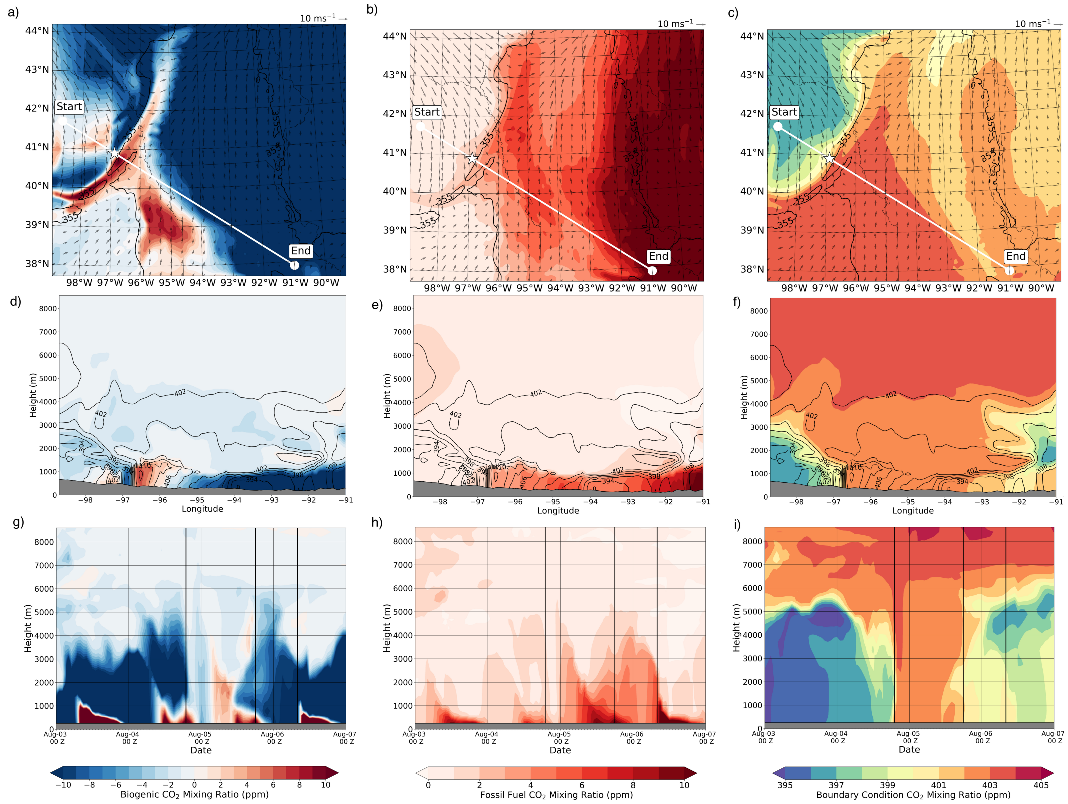

Figure 8. Distribution of CO_2 from various sources in WRF-Chem for the August 4th cold front passage. Panels (a) to (c) show a map of CO_2 from biospheric fluxes within the domain, fossil fuel emissions within the domain, and inflow of CO_2 from the domain boundaries on August 4th 18Z at an altitude of 548m AGL. Panels (d) to (f) show the vertical cross-sections along the transect (white line in panels (a) through (c)) on August 5th at 00Z. Panels (g) to (i) show the time-evolution of CO_2 from various sources over Lincoln, NE from August 3rd to August 7th at 00 UTC. The black contours of total CO_2 mole fractions are shown in panels (a) to (f). The black vertical lines in panels (g) through (i) highlight the period of warm and cold sector passage over the location (as seen in figure 7(b)).

tern and the consequent change in the vertical distribution of CO_2 over the location is attributed to the cold front passage. From the fossil fuel mole fractions shown in figure 8(h), the only significant positive influence (between 4 ppm to 6 ppm) in mole fractions exists between Aug 5th 00Z to Aug 6th 09Z, contributing 7 - 10 ppm/hr to the total near surface change in CO_2 mole fractions. These positive modulations in fossil fuel CO_2 mole fractions reduce sharply towards the end of the frontal passage period after Aug 6th 09Z. The biogenic CO_2 mole fractions are responsible for the diurnal patterns (figure 8(g)) as they represent the uptake of CO_2 by photosynthesis during the day and accumulation due to respiration at night. On Aug 5th at 04Z we see that biogenic CO_2 mole fractions shift from -4 ppm to 4 ppm, coinciding with the warm sector air mass passing over the location.

We find that boundary inflow CO_2 is responsible for roughly 20% of the pre-frontal and frontal near surface difference in CO_2 at this location. During the frontal passage, boundary CO_2 is relatively homogeneous in the vertical distribution, with mole fractions similar to upper free tropospheric values throughout the column. Boundary CO_2 also explains a roughly 3-4 ppm drop in lower free troposphere and ABL CO_2 after frontal passage. The primary driver of the frontal difference is biogenic CO_2, as it explains about 60% of the total change in CO_2 within the ABL between pre-frontal and frontal conditions. Horizontal maps of total CO_2 mole fractions as well as biogenic, fossil fuel and boundary inflow components from Aug 4th 00Z to Aug 5th 06Z at 6-hour intervals are presented in the supporting information section as Figure S2. The maps highlight the changes in cross frontal CO_2 distribution as well as the narrow band of elevated CO_2 as the cold front passes through the domain. The impact of biogenic CO_2 signals on the narrow band of elevated CO_2 along the frontal boundary can clearly be seen on the maps.

We further explore the components of CO_2 within WRF-Chem with a footprint analysis (Figure 9 (c) and (d)) showing the air mass history across the frontal gradient. Simulated particles were released at 300 m above Lincoln, NE on Aug 4th, 20Z (during frontal crossing) and Aug 5th, 03Z (post-frontal crossing). These particles were tracked backwards for 5 days using a Lagrangian particle dispersion model (Uliasz, 1994) and their interactions with the surface were summed to create an influence function of the air measured above Lincoln before and after the frontal crossing. From figure 9(c), we see that the cold sector ABL air at this time and location originated in the southwestern Canada, while the warm sector (figure 9(d)) air came from the south-central region to the south. The biogenic surface fluxes in figure 9(a) are averaged over 5 days and do not quantitatively reflect the impact of the diel variations in fluxes. Studies have shown that meridional gradients in CO_2 mole fractions exist over periods longer than 5 days (Keppel-Aleks et al., 2011). Qualitatively, there is not a large difference in the net biological fluxes in these two upwind areas; neither back trajectory comes from the region of strong net uptake (approximately -9000 $molkm^{-2}hour^{-1}$) to the north and northeast of the flight path. This result is likely to be specific to this frontal case. Since fossil fuel fluxes do not have as strong a diel variability as do biogenic fluxes, the 5-day average better represents the distribution and magnitude of fluxes.

4.4 Mechanism of CO_2 transport along the frontal boundary

Horizontal and vertical advection are the primary transport terms that drive the distribution of CO_2 at the frontal boundary. We compare the three terms driving CO_2 mole fraction gradients in both vertical and horizontal directions (cf. section 2.5) as described in equation (2), which are (*i*) horizontal advection, (*ii*) vertical advection and (*iii*) vertical diffusion. Figure 10 shows the transport terms along the transect shown in figure 6(b). Since this figure represents a snapshot in time, the sign of the transport term does not reflect its influence for the period of frontal passage. Overall, horizontal advection is strongest near the frontal boundary and a positive influence in the warm sector. The magnitude of horizontal advection is greatest at the frontal boundary, where

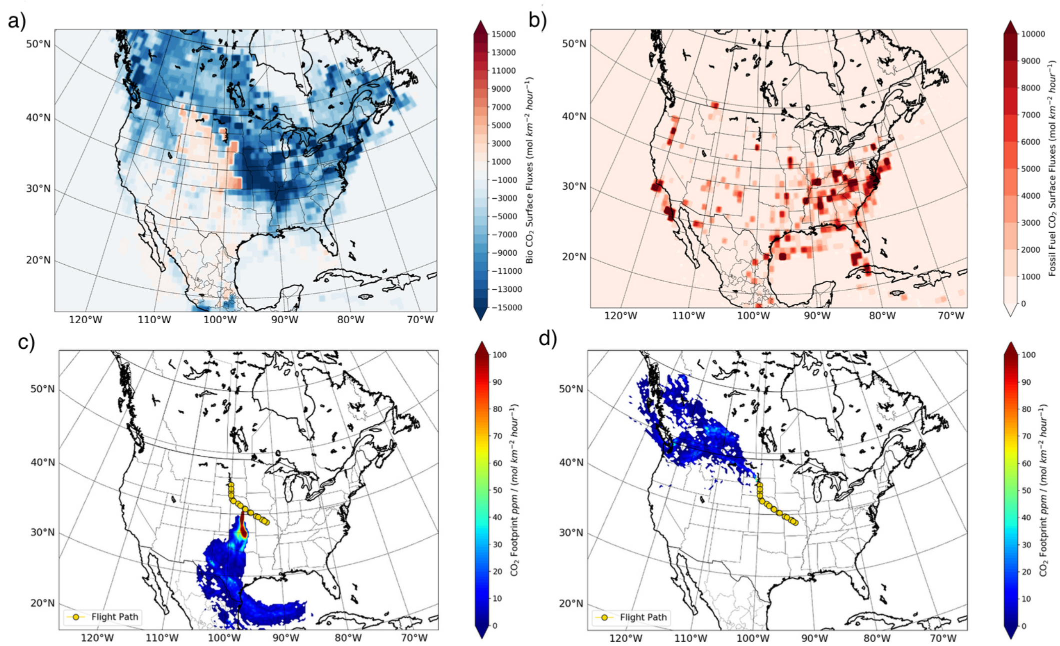

Figure 9. Footprint analysis of air mass along the frontal boundary showing the surface fluxes from CT-NRT.v2017 and regions of influence. Panel(a) has biogenic CO_2 surface fluxes and panel (b) shows fossil fuel CO_2 surface fluxes. The surface flux maps have been averaged over 5 days. Panel (c) shows the air mass history for the warm air mass ahead of the front and panel (d) shows the air mass history for the cold air mass behind the front. The flight path is shows as yellow circles.

the CO_2 mole fraction gradient is the strongest. As seen in figure 10(a), horizontal advection has a high magnitude ($\sim$ 10 ppm/hr) in the ABL at the warm sector of the frontal boundary (between -97° and -96° longitude). Near surface values of horizontal advection have positive values in the warm sector and negative values of similar magnitude in the cold sector. Alternating negative and positive values can be interpreted as transport of CO_2 from a depleted region followed by an elevated CO_2 region due to changes in the direction of the CO_2 flow as the cold front propagates. Further into the warm sector (Figure 6(b)) of the front, there is a region of accumulation caused by horizontal advection between -96° and -94° longitude . However, the magnitudes are not as high as those near the frontal boundary.

The influence of vertical advection on the distribution of CO_2 across the front is generally restricted to the region close to the frontal boundary (between -97° and -95° longitude) as seen in figure 10(b). However, unlike horizontal advection, the magnitude of vertical advection is significantly lower than horizontal advection (2 ppm/hr compared to 10 ppm/hr) as seen in figure 10(b). While vertical advection has a very low magnitude in figure 10(b), horizontal maps of vertical advection at multiple levels show the significant transport just above the ABL. These maps are shown as Figure S1 in the supporting information section.

Vertical diffusion has a significantly smaller magnitude than the advection terms - contributing less than 2×10^{-3} ppm/hr to the total CO_2 transport during the frontal passage period. Thus, for this cold front passage, horizontal advection is the primary transport term active near the frontal boundary and in the warm sector as well. The magnitude of the transport terms are greatest in the ABL , and drop to smaller values (around 1-2 ppm/hr) in the free troposphere. Based on the cross-section shown in figure 10, horizontal advection accounts for most of the total CO_2 transport while vertical advection contributes to CO_2 transport especially near the top of the ABL

Evolution of the vertical distribution of transport budget terms over a location shows that the terms have the greatest magnitude at the beginning of frontal influence and at the frontal boundary between the warm and cold sectors. In figure 11(a), the vertical distribution of horizontal advection over the reference location is shown from August 3rd to August 7th 00Z. At the start of the frontal influence around Aug 4th 18Z, there is a sharp increase in the magnitude of horizontal advection with negative influence in the boundary layer (-10 ppm/hr). This increase in magnitude is restricted to the ABL. Between 2km to 3km MSL, there is a positive (2 ppm/hr) region. The abrupt change in signs near Aug 4th 18Z can be attributed to the change in air masses due to introduction of the warm sector (Figure 11 (a)) over the region. Simultaneously, the distribution of vertical advection is shown in figure 11(b). Unlike horizontal advection, vertical advection does not show strong ($>$ 8 ppm/hr) near surface influences during the pre-frontal period (apart from the nocturnal buildup). During the initial period of frontal influence, vertical advection has reduced ($<$ 4 ppm/hr) influence under 1km MSL. The distribution above 1km MSL is similar to horizontal advection. The frontal boundary separating the warm and cold sectors passes over the location around Aug 5th 18Z.

Vertical advection has significant magnitude in the ABL during the nocturnal buildup period and when the frontal influence is present over the location between Aug 4th 18Z and Aug 6th 00Z as seen in figure 11(b). From figure 11(a) and (b) it can be seen that during the warm sector period from Aug 4th 18Z to Aug 5th 00Z, there is an overlap of vertical and horizontal advection in the ABL as well as the lower free troposphere. Within the ABL, vertical advection has the opposing impact compared to horizontal advection. Dynamically speaking, vertical advection lifts air mass with elevated CO_2 to regions with lower CO_2 mole fractions, thereby causing accumulation in the vertical distribution of CO_2. Horizontal advection carries this air mass with increased CO_2 mole fractions into air with lower mole fractions and depletes the combined CO_2 mole fractions. As the frontal boundary passes over the location (between Aug 5th 18Z and Aug 6th 18Z), based on

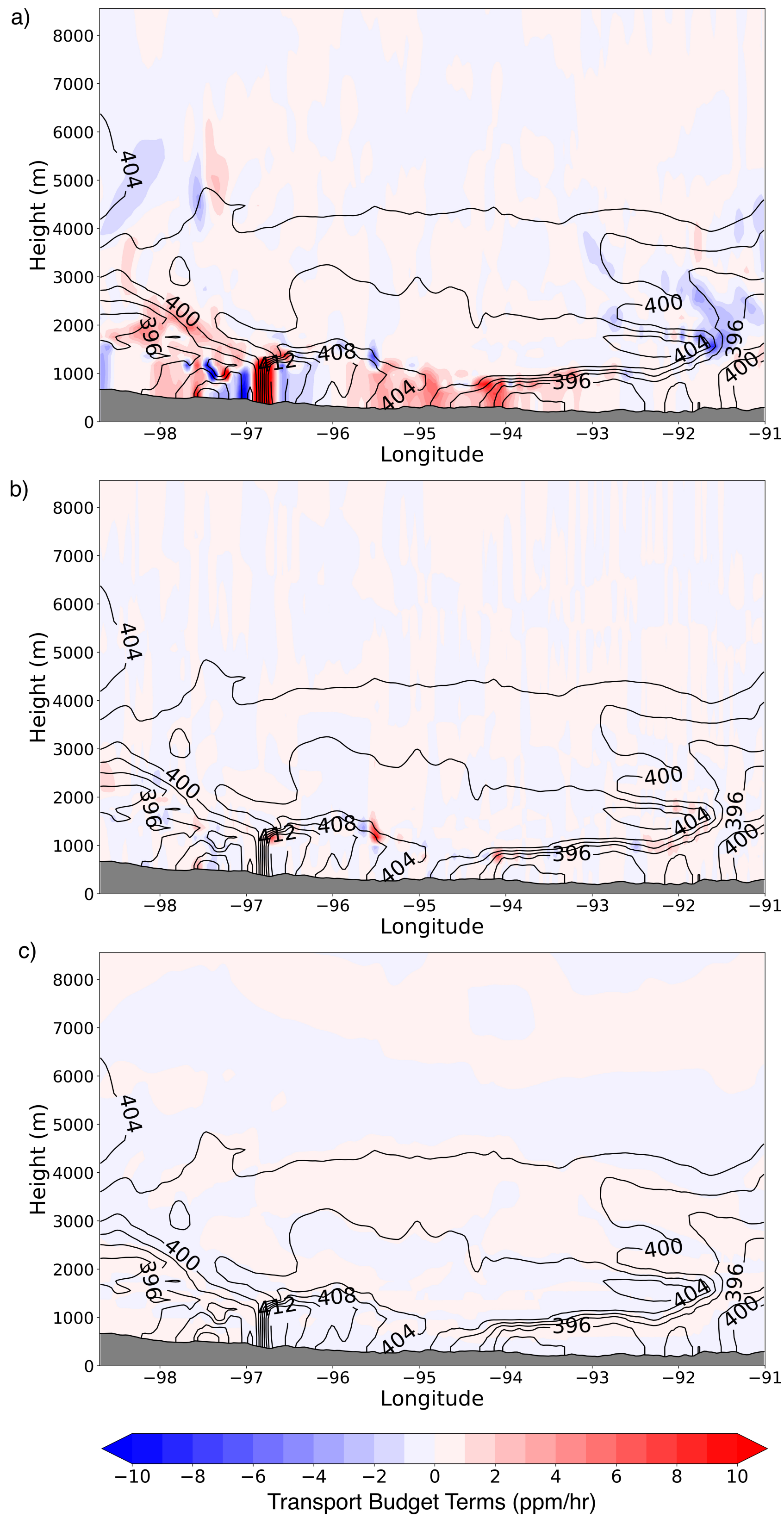

Figure 10. Transport processes impacting CO_2 distribution across the frontal boundary on August 4th at 18Z along the transect shown in figure 6(b). The colored contours show the transport terms while the black contour lines represent the corresponding CO_2 mole fractions. Panel (a) shows horizontal advection, panel (b) shows vertical advection and panel (c) shows vertical diffusion.

figure 10 and 11, it can be seen that majority of the boundary layer CO_2 transport in the cold sector of the front is driven by horizontal transport.

Vertical diffusion does not show any transport in the same order of magnitude as the advection terms throughout the period from Aug 3rd 00Z to Aug 7th 00Z. From figure 11(c) we see that there is no change in magnitude of the vertical diffusion term throughout the period of frontal influence over the location.

In summary, horizontal advection is the primary transport mechanism during the frontal period. For horizontal advection and vertical advection, the impact during frontal passages differ from non-frontal periods. In comparison, vertical diffusion is not affected by the cold front passage. Based on the sign of the terms as well the region and period of influence, horizontal and vertical advection show a coupled transport impact during the warm sector of the frontal passage period.

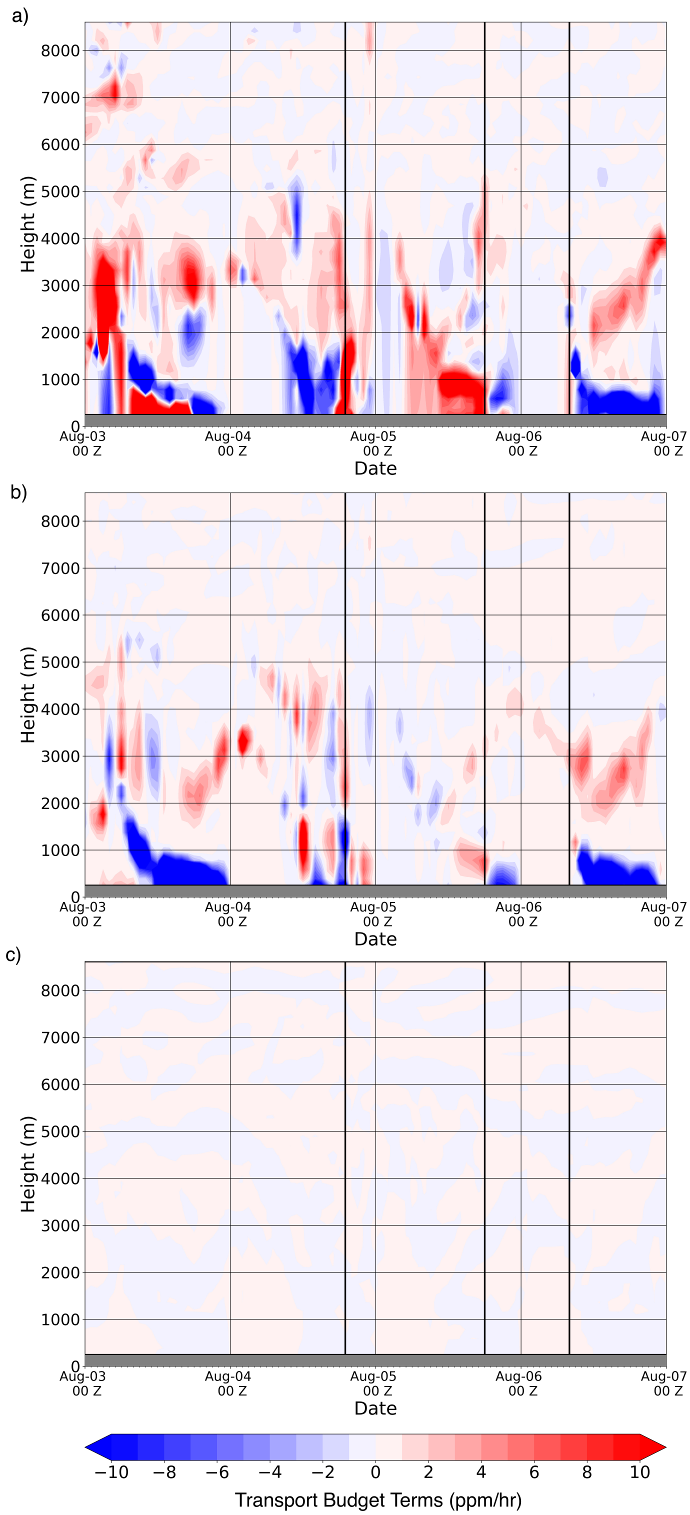

Figure 11. Evolutions of transport terms impacting CO_2 distribution across the frontal boundary from August 3rd to August 7th at 00Z over the reference location in Nebraska as shown in figure 6(b). The vertical black lines show the period of frontal influence from Aug 4th 18Z to Aug 6th 09Z over the reference location. Panel (a) shows horizontal advection, panel (b) shows vertical advection and panel (c) shows vertical diffusion. The black vertical lines highlight the period of warm and cold sector passage over the location (as seen in figure 7(b)).

5 Discussion and conclusions

In this study, we presented findings from a cloud resolving resolution simulation of a cold front passage on August 4th over Lincoln, Nebraska in the Mid-West region of United States. The performance of the WRF-Chem setup used was evaluated using aircraft measurements from the NASA ACT-America 2016 campaign. In order to understand the changes in atmospheric CO_2 mole fractions during the cold front passage, we showed the contribution of biogenic and fossil fuel sources along with large scale inflow from the domain boundaries. Using a modified form of a CO_2 budget equation (Bakwin et al., 2004; Parazoo et al., 2008), we quantified the interaction of horizontal advection, vertical advection, and vertical diffusion with CO_2 mole fractions during the cold front passage.

Focusing on a single cold front passage, we were able to simulate the changes in the distribution of CO_2 on both sides of the cold front. We found that the cold sector of the front had air mass with lower CO_2 mole fractions (< 400 ppm) compared to the warm sector (> 405 ppm). The presence of horizontal gradients in CO_2 mole fractions across the frontal boundary was consistent with previous studies (Hurwitz et al., 2004; Wang et al., 2007). In addition to the large scale difference in CO_2 mole fractions across the frontal boundary, we also found the presence of a narrow band of air mass with elevated CO_2 mole fractions located along the frontal boundary extending into the warm sector. This air mass had the highest CO_2 mole fractions (> 410 ppm) and was distinct from the warm sector air mass surrounding it. The simulated CO_2 enhancement had a similar magnitude to aircraft measurements and the location of the enhanced CO_2 region was located further to the northwest in aircraft measurements. While previous studies have linked observed increases in CO_2 mole fractions associated with a cold front passage to anomalies created due to wind flow deformation and shear (Lee et al., 2012), in this study, we have presented the horizontal and vertical extent of this feature. Through the decomposition of CO_2 mole fractions into its source regions, we found that the cold sector air mass originated over southwestern Canada, while the warm sector air mass originated over the Gulf of Mexico. The changes in CO_2 mole fractions during the frontal passage can be attributed to a large scale difference in CO_2 mole fractions between the warm and cold sector air masses along with the elevated CO_2 mole fractions along the frontal boundary. By decomposing atmospheric CO_2 mole fractions into source based components, we found that the large scale gradient was represented in the boundary inflow as well as the local (within domain) biogenic CO_2 component. The elevated CO_2 mole fractions along the frontal boundary were driven by biogenic CO_2 mole fractions from within the domain. Similar to Chan et al. (2004), we also found that the interaction of CO_2 mole fractions from biogenic sources with horizontal and vertical advection is the primary driver of CO_2 gradients during the cold front passage. Using the the CO_2 budget equation (Parazoo et al., 2008; Bakwin et al., 2004), we found that horizontal advection is the dominant transport mechanism during the cold front passage, while vertical advection plays an important role near the frontal boundary in the warm sector. We have shown a detailed analysis of transport processes for a single frontal passage case study using a high resolution numerical model capable of resolving most of the vertical transport near the frontal boundary. We found that during the cold front passage, gradients in CO_2 mole fractions were advected into the region through the boundary inflow component as also seen in Geels et al. (2004). These boundary inflow gradients extended from the surface to 5000m AGL.

We highlight the main conclusions from our study on CO_2 distribution, origins, and transport along a frontal boundary for the August 4th cold front passage as follows:

1. Using high-resolution WRF-Chem simulations, we showed an elongated band of elevated (> 410 ppm) CO_2 mole fractions along the frontal boundary. This band was captured in aircraft measurements as a part of the ACT-America flight cam-

   paign as well (Pal et al., 2020; Davis et al., 2018). The role of this feature in determining the continental scale transport of CO_2 remains unclear and is worthy of additional study.

2. We found that CO_2 introduced into our domain by horizontal advection as boundary inflow had horizontal and vertical gradients along the frontal boundary. These gradients were weaker than those observed near the frontal boundary. Our study quantitatively showed that combining local biogenic and fossil fuel CO_2 mole fractions to the boundary CO_2 resulted in gradients similar to observations.
3. At a cloud-resolving resolution of 3km, our study was able to capture the vertical transport of CO_2 at the frontal boundary in greater detail compared to previous studies with coarser resolutions - this improvement in representation of physical processes due to increase in resolution has previously been shown in air quality and convective precipitation studies (Li et al., 2019; Ekström & Gilleland, 2017). Near the frontal boundary, in the warm sector, where the gradients in CO_2 are strongest, horizontal and vertical advection have comparable magnitudes.
4. We also showed fractional contributions to cross frontal CO_2 differences in the boundary layer and free troposphere from each component (biogenic, fossil fuel, and boundary inflow). For the August 4th cold front passage, biogenic CO_2 was the primary driver of the narrow band of elevated CO_2 along the frontal boundary. Boundary inflow along with biogenic CO_2 were the major contributors to the cross frontal CO_2 difference. The evolution of the narrow band and the cross frontal difference was shown over multiple days as the cold front passed over the region - highlighting the distinct impact of frontal passage on local CO mole fractions.

Through this body of work, we aim to provide information about CO_2 transport during cold front passages, especially for future aircraft campaigns like ACT-America and other field experiments involving CO_2 distribution by synoptic scale events. A caveat of our study was that it was limited to only one frontal passage event and thus, a general theory on the impact of fronts cannot be established. Future work should be able to incorporate multiple frontal passages over a region. The presence of the elongated band of CO_2 along the frontal boundary can be tested for multiple events. Repeatable patterns of horizontal and vertical transport as seen in this case can be tested and quantified.

Acknowledgments

Primary funding for this research was provided by NASA's Earth Sciences Division as part of the Atmospheric Carbon and Transport (ACT)America Earth Venture Suborbital mission (grant NNX15AG76G to Penn State). ACT-America aircraft datasets for this research are available at Oak Ridge National Laboratory DAAC (Davis et al., 2018). We thank M. P. Butler at the Pennsylvania State University for generating the codes that incorporate the global modeled CO_2 mole fractions into the regional model with the conservation of mass (Lauvaux, 2020). CarbonTracker (CT-NRTv2017x) results were provided by NOAA ESRL, Boulder, Colorado, United States, from the website at http://carbontracker.noaa.gov.

Computing resources were provided by the NASA HighEnd Computing (HEC) Program through the NASA Advanced Supercomputing (NAS) Division at Ames Research Center. The WRFChem model output used for the current study is available at datacommons.psu.edu.

References

Agustí-Panareda, A., Diamantakis, M., Massart, S., Chevallier, F., Muñoz-Sabater, J., Barré, J., … Wunch, D. (2019). Modelling CO₂

weather – why horizontal resolution matters. *Atmospheric Chemistry and Physics Discussions*, 1–48. doi: 10.5194/acp-2019-177

Bakwin, P. S., Davis, K. J., Yi, C., Wofsy, S. C., Munger, J. W., Haszpra, L., & Barcza, Z. (2004, 1). Regional carbon dioxide fluxes from mixing ratio data. *Tellus B: Chemical and Physical Meteorology*, *56*(4), 301–311. Retrieved from `https://www.tandfonline.com/doi/full/10.3402/tellusb.v56i4.16446` doi: 10.3402/tellusb.v56i4.16446

Ballav, S., Patra, P. K., Takigawa, M., Ghosh, S., De, U. K., Maksyutov, S., ... Hashimoto, S. (2012). Simulation of CO2 Concentration over East Asia Using the Regional Transport Model WRF-CO2. *Journal of the Meteorological Society of Japan. Ser. II*, *90*(6), 959–976. Retrieved from `http://jlc.jst.go.jp/DN/JST.JSTAGE/jmsj/2012-607?lang=en&from=CrossRef&type=abstract` doi: 10.2151/jmsj.2012-607

Bastos, A., O'Sullivan, M., Ciais, P., Makowski, D., Sitch, S., Friedlingstein, P., ... Zaehle, S. (2020, 2). Sources of Uncertainty in Regional and Global Terrestrial CO 2 Exchange Estimates. *Global Biogeochemical Cycles*, *34*(2), 1–21. Retrieved from `https://onlinelibrary.wiley.com/doi/abs/10.1029/2019GB006393` doi: 10.1029/2019GB006393

Berrisford, P., Kållberg, P., Kobayashi, S., Dee, D., Uppala, S., Simmons, A. J., ... Sato, H. (2011). Atmospheric conservation properties in ERA-Interim. *Quarterly Journal of the Royal Meteorological Society*, *137*(659), 1381–1399. Retrieved from `http://dx.doi.org/10.1002/qj.864` doi: 10.1002/qj.864

Butler, M. P., Lauvaux, T., Feng, S., Liu, J., Bowman, K. W., & Davis, K. J. (2020, 7). Atmospheric Simulations of Total Column CO2 Mole Fractions from Global to Mesoscale within the Carbon Monitoring System Flux Inversion Framework. *Atmosphere 2020, Vol. 11, Page 787*, *11*(8), 787. Retrieved from `https://www.mdpi.com/779918` doi: 10.3390/ATMOS11080787

Carvalho, D., Rocha, A., Gómez-Gesteira, M., & Silva Santos, C. (2014). Comparison of reanalyzed, analyzed, satellite-retrieved and NWP modelled winds with buoy data along the Iberian Peninsula coast. *Remote Sensing of Environment*, *152*, 480–492. doi: 10.1016/j.rse.2014.07.017

Chan, D., Yuen, C. W., Higuchi, K., Shashkov, A., Liu, J., Chen, J., & Worthy, D. (2004, 1). On the CO 2 exchange between the atmosphere and the biosphere: the role of synoptic and mesoscale processes. *Tellus B: Chemical and Physical Meteorology*, *56*(3), 194–212. Retrieved from `https://www.tandfonline.com/doi/full/10.3402/tellusb.v56i3.16424` doi: 10.3402/tellusb.v56i3.16424

Chen, F., & Dudhia, J. (2001). Coupling an Advanced Land SurfaceHydrology Model with the Penn StateNCAR MM5 Modeling System. Part I: Model Implementation and Sensitivity. *Monthly Weather Review*, *129*(4), 569–585. Retrieved from `http://dx.doi.org/10.1175/1520-0493(2001)129%3C0569:CAALSH%3E2.0.CO%5Cn2` doi: 10.1175/1520-0493(2001)129⟨0569:CAALSH⟩2.0.CO;2

Chen, H. W., Zhang, L. N., Zhang, F., Davis, K. J., Lauvaux, T., Pal, S., ... DiGangi, J. P. (2019, 7). Evaluation of Regional CO 2 Mole Fractions in the ECMWF CAMS RealTime Atmospheric Analysis and NOAA CarbonTracker NearRealTime Reanalysis With Airborne Observations From ACTAmerica Field Campaigns. *Journal of Geophysical Research: Atmospheres*, *124*(14), 8119–8133. Retrieved from `https://onlinelibrary.wiley.com/doi/abs/10.1029/2018JD029992` doi: 10.1029/2018JD029992

Chevallier, F., Remaud, M., O'Dell, C. W., Baker, D., Peylin, P., & Cozic, A. (2019, 11). Objective evaluation of surface- and satellite-driven carbon dioxide atmospheric inversions. *Atmospheric Chemistry and Physics*, *19*(22), 14233–14251. Retrieved from `https://acp.copernicus.org/articles/19/14233/2019/` doi: 10.5194/acp-19-14233-2019

Davis, K. J., Obland, M. D., Lin, B., Lauvaux, T., O'Dell, C. W., Meadows, B., ... Nehrir, A. R. (2018). *ACT-America: L3 Merged In Situ Atmospheric Trace Gases and Flask Data, Eastern USA.* ORNL Distributed Active Archive Center. Retrieved from https://daac.ornl.gov/cgi-bin/dsviewer.pl?ds_id=1593 doi: 10.3334/ORNLDAAC/1593

Dee, D. P., Uppala, S. M., Simmons, A. J., Berrisford, P., Poli, P., Kobayashi, S., ... Vitart, F. (2011, 4). The ERA-Interim reanalysis: configuration and performance of the data assimilation system. *Quarterly Journal of the Royal Meteorological Society*, *137*(656), 553–597. Retrieved from http://doi.wiley.com/10.1002/qj.828 doi: 10.1002/qj.828

Denning, a. S., Fung, I. Y., & Randall, D. (1995). *Latitudinal gradient of atmospheric CO2 due to seasonal exchange with land biota* (Vol. 376) (No. 6537). doi: 10.1038/376240a0

Díaz-Isaac, L., Lauvaux, T., & Davis, K. (2018, 10). Impact of physical parameterizations and initial conditions on simulated atmospheric transport and CO2 mole fractions in the US Midwest. *Atmospheric Chemistry and Physics*, *18*(20), 14813–14835. Retrieved from https://www.atmos-chem-phys.net/18/14813/2018/ doi: 10.5194/acp-18-14813-2018

Díaz Isaac, L. I., Lauvaux, T., Davis, K. J., Miles, N. L., Richardson, S. J., Jacobson, A. R., & Andrews, A. E. (2014, 9). Model-data comparison of MCI field campaign atmospheric CO 2 mole fractions. *Journal of Geophysical Research: Atmospheres*, *119*(17), 10536–10551. Retrieved from https://doi.org/10.1002/2014JD021593http://doi.wiley.com/10.1002/2014JD021593 doi: 10.1002/2014JD021593

Digangi, J. P., Choi, Y., Nowak, J. B., Halliday, H. S., & Yang, M. M. (2018). *ACT-America: L2 In Situ Atmospheric CO2, CO, CH4, and O3 Concentrations, Eastern USA.* ORNL Distributed Active Archive Center. Retrieved from https://daac.ornl.gov/cgi-bin/dsviewer.pl?ds_id=1556 doi: 10.3334/ORNLDAAC/1556

Edenhofer, O., Pichs-Madruga, R., Sokona, Y., Kadner, S., Minx, J. C., Brunner, S., ... Zwickel, T. (2014). Climate Change 2014 Mitigation of Climate Change. In *Working group iii contribution to the fifth assessment report of the intergovernmental panel on climate change* (p. 1454). Cambridge: Cambridge University Press. Retrieved from http://www.ipcc.ch/report/ar5/wg3/%0Ahttp://ebooks.cambridge.org/ref/id/CBO9781107415416http://ebooks.cambridge.org/ref/id/CBO9781107415416 doi: 10.1017/CBO9781107415416

Ekström, M., & Gilleland, E. (2017, 1). Assessing convection permitting resolutions of WRF for the purpose of water resource impact assessment and vulnerability work: A southeast Australian case study. *Water Resources Research*, *53*(1), 726–743. Retrieved from https://doi.org/10.1002/2016WR019545 doi: 10.1002/2016WR019545

Enting, I. G., Trudinger, C. M., & Francey, R. J. (1995, 2). A synthesis inversion of the concentration and delta13 C of atmospheric CO2. *Tellus B*, *47*(1-2), 35–52. Retrieved from http://www.tellusb.net/index.php/tellusb/article/view/15998 doi: 10.1034/j.1600-0889.47.issue1.5.x

Feng, S., Lauvaux, T., Davis, K. J., Keller, K., Zhou, Y., Williams, C., ... Baker, I. (2019, 12). Seasonal Characteristics of Model Uncertainties From Biogenic Fluxes, Transport, and Large-Scale Boundary Inflow in Atmospheric CO2 Simulations Over North America. *Journal of Geophysical Research: Atmospheres*, *124*(24), 14325–14346. Retrieved from https://doi.org/10.1029/2019JD031165 doi: 10.1029/2019JD031165

Feng, S., Lauvaux, T., Keller, K., Davis, K. J., Rayner, P., Oda, T., & Gurney, K. R. (2019, 11). A Road Map for Improving the Treatment of Uncertainties in High-Resolution Regional Carbon Flux Inverse Estimates. *Geophysical*

Research Letters, *46*(22), 13461–13469. Retrieved from https://doi.org/10.1029/2019GL082987 doi: 10.1029/2019GL082987

Feng, S., Lauvaux, T., Newman, S., Rao, P., Ahmadov, R., Deng, A., . . . Yung, Y. L. (2016). LA Megacity: a High-Resolution Land-Atmosphere Modelling System for Urban CO₂ Emissions. *Atmospheric Chemistry and Physics Discussions*(March), 1–56. Retrieved from http://www.atmos-chem-phys-discuss.net/acp-2016-143/ doi: 10.5194/acp-2016-143

Friedlingstein, P., Jones, M. W., O'Sullivan, M., Andrew, R. M., Hauck, J., Peters, G. P., . . . Zaehle, S. (2019, 12). Global Carbon Budget 2019. *Earth System Science Data*, *11*(4), 1783–1838. Retrieved from https://essd.copernicus.org/articles/11/1783/2019/ doi: 10.5194/essd-11-1783-2019

Geels, C., Doney, S. C., Dargaville, R., Brandt, J., & Christensen, J. H. (2004, 1). Investigating the sources of synoptic variability in atmospheric CO 2 measurements over the Northern Hemisphere continents: a regional model study. *Tellus B: Chemical and Physical Meteorology*, *56*(1), 35–50. Retrieved from https://www.tandfonline.com/doi/full/10.3402/tellusb.v56i1.16399 doi: 10.3402/tellusb.v56i1.16399

Geels, C., Gloor, M., Ciais, P., Bousquet, P., Peylin, P., Vermeulen, A. T., . . . Santaguida, R. (2007, 7). Comparing atmospheric transport models for future regional inversions over Europe – Part 1: mapping the atmospheric CO¡sub¿2¡/sub¿ signals. *Atmospheric Chemistry and Physics*, *7*(13), 3461–3479. Retrieved from http://www.atmos-chem-phys.net/7/3461/2007/ doi: 10.5194/acp-7-3461-2007

Gurney, K. R., Law, R. M., Denning, A. S., Rayner, P. J., Baker, D., Bousquet, P., . . . Yuen, C.-W. (2002, 2). Towards robust regional estimates of CO2 sources and sinks using atmospheric transport models. *Nature*, *415*(6872), 626–630. Retrieved from https://doi.org/10.1038/415626ahttps://www.nature.com/articles/415626a#supplementary-informationhttp://www.nature.com/articles/415626a doi: 10.1038/415626a

Houghton, R. A., House, J. I., Pongratz, J., van der Werf, G. R., DeFries, R. S., Hansen, M. C., . . . Ramankutty, N. (2012, 12). Carbon emissions from land use and land-cover change. *Biogeosciences*, *9*(12), 5125–5142. Retrieved from https://www.biogeosciences.net/9/5125/2012/ doi: 10.5194/bg-9-5125-2012

Houweling, S., Aben, I., Breon, F. M., Chevallier, F., Deutscher, N., Engelen, R., . . . Serrar, S. (2010). The importance of transport model uncertainties for the estimation of CO2 sources and sinks using satellite measurements. *Atmospheric Chemistry and Physics*, *10*(20), 9981–9992. doi: 10.5194/acp-10-9981-2010

Huntzinger, D. N., Michalak, A. M., Schwalm, C., Ciais, P., King, A. W., Fang, Y., . . . Zhao, F. (2017, 12). Uncertainty in the response of terrestrial carbon sink to environmental drivers undermines carbon-climate feedback predictions. *Scientific Reports*, *7*(1), 4765. Retrieved from http://www.nature.com/articles/s41598-017-03818-2 doi: 10.1038/s41598-017-03818-2

Hurwitz, M. D., Ricciuto, D. M., Bakwin, P. S., Davis, K. J., Wang, W., Yi, C., & Butler, M. P. (2004). Transport of Carbon Dioxide in the Presence of Storm Systems over a Northern Wisconsin Forest. *Journal of the Atmospheric Sciences*, *61*(5), 607–618. doi: 10.1175/1520-0469(2004)061⟨0607:TOCDIT⟩2.0.CO;2

Iacono, M. J., Delamere, J. S., Mlawer, E. J., Shephard, M. W., Clough, S. A., & Collins, W. D. (2008). Radiative forcing by long-lived greenhouse gases: Calculations with the AER radiative transfer models. *Journal of Geophysical Research: Atmospheres*, *113*(D13), n/a-n/a. Retrieved from http://dx.doi.org/10.1029/2008JD009944 doi: 10.1029/2008JD009944

Kain, J. S. (2004). The KainFritsch Convective Parameterization: An Update. *Journal of Applied Meteorology*, *43*(1), 170–181. Retrieved from http://journals.ametsoc.org/doi/abs/10.1175/1520-0450(2004)043%3C0170:TKCPAU%3E2.0.CO;2 doi: 10.1175/1520-0450(2004)043⟨0170:TKCPAU⟩2.0.CO;2

Keppel-Aleks, G., Wennberg, P. O., & Schneider, T. (2011, 4). Sources of variations in total column carbon dioxide. *Atmospheric Chemistry and Physics*, *11*(8), 3581–3593. Retrieved from https://acp.copernicus.org/articles/11/3581/2011/ doi: 10.5194/acp-11-3581-2011

Klemp, J. B. (2006, 1). Advances in the WRF model for convection-resolving forecasting. *Advances in Geosciences*, *7*, 25–29. Retrieved from http://www.adv-geosci.net/7/25/2006/ doi: 10.5194/adgeo-7-25-2006

Lauvaux, T. (2020, 5). *psu-inversion/WRF_boundary_coupling: WRF Boundary Coupling (Tracer mode - Chemistry).* Retrieved from https://zenodo.org/record/3832214 doi: 10.5281/ZENODO.3832214

Lauvaux, T., & Davis, K. J. (2014, 1). Planetary boundary layer errors in mesoscale inversions of column-integrated CO 2 measurements. *Journal of Geophysical Research: Atmospheres*, *119*(2), 490–508. Retrieved from http://doi.wiley.com/10.1002/2013JD020175 doi: 10.1002/2013JD020175

Lauvaux, T., Schuh, A. E., Uliasz, M., Richardson, S., Miles, N., Andrews, A. E., … Davis, K. J. (2012, 1). Constraining the CO₂ budget of the corn belt: exploring uncertainties from the assumptions in a mesoscale inverse system. *Atmospheric Chemistry and Physics*, *12*(1), 337–354. Retrieved from https://www.atmos-chem-phys.net/12/337/2012/ doi: 10.5194/acp-12-337-2012

Law, R. M., Peters, W., Rödenbeck, C., Aulagnier, C., Baker, I., Bergmann, D. J., … Zhu, Z. (2008, 9). TransCom model simulations of hourly atmospheric CO 2 : Experimental overview and diurnal cycle results for 2002. *Global Biogeochemical Cycles*, *22*(3), n/a-n/a. Retrieved from http://doi.wiley.com/10.1029/2007GB003050 doi: 10.1029/2007GB003050

Law, R. M., Rayner, P. J., Denning, A. S., Erickson, D., Fung, I. Y., Heimann, M., … Watterson, I. G. (1996). *Variations in modeled atmospheric transport of carbon dioxide and the consequences for CO 2 inversions* (Vol. 10) (No. 4). doi: 10.1029/96GB01892

Lee, T. R., De Wekker, S. F., Andrews, A. E., Kofler, J., & Williams, J. (2012, 1). Carbon dioxide variability during cold front passages and fair weather days at a forested mountaintop site. *Atmospheric Environment*, *46*, 405–416. Retrieved from http://www.sciencedirect.com/science/article/pii/S1352231011010314https://linkinghub.elsevier.com/retrieve/pii/S1352231011010314 doi: 10.1016/j.atmosenv.2011.09.068

Le Quéré, C., Andrew, R. M., Friedlingstein, P., Sitch, S., Hauck, J., Pongratz, J., … Zheng, B. (2018, 12). Global Carbon Budget 2018. *Earth System Science Data*, *10*(4), 2141–2194. Retrieved from https://www.earth-syst-sci-data-discuss.net/essd-2017-123/https://essd.copernicus.org/articles/10/2141/2018/ doi: 10.5194/essd-10-2141-2018

Li, Y., Barth, M. C., & Steiner, A. L. (2019). Comparing turbulent mixing of atmospheric oxidants across model scales. *Atmospheric Environment*, *199*, 88–101. Retrieved from http://www.sciencedirect.com/science/article/pii/S1352231018307702 doi: https://doi.org/10.1016/j.atmosenv.2018.11.004

Nakanishi, M., & Niino, H. (2006). An improved Mellor-Yamada Level-3 model: Its numerical stability and application to a regional prediction of advection fog. *Boundary-Layer Meteorology*, *119*(2), 397–407. doi: 10.1007/s10546-005-9030-8

Pal, S., Davis, K. J., Lauvaux, T., Browell, E. V., Gaudet, B. J., Stauffer, D. R., … Zhang, F. (2020, 3). Observations of Greenhouse Gas Changes Across Summer Frontal Boundaries in the Eastern United States. *Journal of Geo-*

physical Research: Atmospheres, *125*(5), e2019JD030526. Retrieved from `https://doi.org/10.1029/2019JD030526https://onlinelibrary.wiley.com/doi/abs/10.1029/2019JD030526` doi: 10.1029/2019JD030526

Parazoo, N. C., Denning, A. S., Kawa, S. R., Corbin, K. D., Lokupitiya, R. S., & Baker, I. T. (2008). Mechanisms for synoptic variations of atmospheric CO2 in North America, South America and Europe. *Atmospheric Chemistry and Physics*, *8*(23), 7239–7254. Retrieved from `http://www.atmos-chem-phys.net/8/7239/2008/` doi: 10.5194/acp-8-7239-2008

Patra, P. K., Law, R. M., Peters, W., Rödenbeck, C., Takigawa, M., Aulagnier, C., ... Zhu, Z. (2008, 12). TransCom model simulations of hourly atmospheric CO 2 : Analysis of synoptic-scale variations for the period 2002-2003. *Global Biogeochemical Cycles*, *22*(4), n/a-n/a. Retrieved from `http://doi.wiley.com/10.1029/2007GB003081` doi: 10.1029/2007GB003081

Pauluis, O., Czaja, A., & Korty, R. (2008, 8). The global atmospheric circulation on moist isentropes. *Science*, *321*(5892), 1075–1078. doi: 10.1126/science.1159649

Peters, W., Jacobson, A. R., Sweeney, C., Andrews, A. E., Conway, T. J., Masarie, K., ... Tans, P. P. (2007, 11). An atmospheric perspective on North American carbon dioxide exchange: CarbonTracker. *Proceedings of the National Academy of Sciences*, *104*(48), 18925–18930. Retrieved from `http://www.pnas.org/content/104/48/18925.abstract` doi: 10.1073/pnas.0708986104

Peylin, P., Baker, D., Sarmiento, J., Ciais, P., & Bousquets, P. (2002). Influence of transport uncertainty on annual mean and seasonal inversions of atmospheric CO2 data. *Journal of Geophysical Research Atmospheres*, *107*(19), 4385. Retrieved from `http://doi.wiley.com/10.1029/2001JD000857` doi: 10.1029/2001JD000857

Sarrat, C., Noilhan, J., Dolman, A. J., Gerbig, C., Ahmadov, R., Tolk, L. F., ... Donier, S. (2007, 12). Atmospheric CO¡sub¿2¡/sub¿ modeling at the regional scale: an intercomparison of 5 meso-scale atmospheric models. *Biogeosciences*, *4*(6), 1115–1126. Retrieved from `http://www.biogeosciences.net/4/1115/2007/` doi: 10.5194/bg-4-1115-2007

Schuh, A. E., Jacobson, A. R., Basu, S., Weir, B., Baker, D., Bowman, K., ... Palmer, P. I. (2019, 4). Quantifying the Impact of Atmospheric Transport Uncertainty on CO 2 Surface Flux Estimates. *Global Biogeochemical Cycles*, *33*(4), 484–500. Retrieved from `https://onlinelibrary.wiley.com/doi/abs/10.1029/2018GB006086` doi: 10.1029/2018GB006086

Skamarock, W., Klemp, J., Dudhi, J., Gill, D., Barker, D., Duda, M., ... Powers, J. (2008). A Description of the Advanced Research WRF Version 3. *Technical Report*(June), 113. doi: 10.5065/D6DZ069T

Skeie, R. B., Berntsen, T. K., Myhre, G., Tanaka, K., Kvalevåg, M. M., & Hoyle, C. R. (2011, 11). Anthropogenic radiative forcing time series from pre-industrial times until 2010. *Atmospheric Chemistry and Physics*, *11*(22), 11827–11857. Retrieved from `https://www.atmos-chem-phys.net/11/11827/2011/` doi: 10.5194/acp-11-11827-2011

Tans, P. P., Fung, I. Y., & Takahashi, T. (1990, 3). Observational Contrains on the Global Atmospheric Co₂ Budget. *Science*, *247*(4949), 1431 LP - 1438. Retrieved from `http://science.sciencemag.org/content/247/4949/1431.abstract` doi: 10.1126/science.247.4949.1431

Thompson, G., Field, P. R., Rasmussen, R. M., & Hall, W. D. (2008). Explicit Forecasts of Winter Precipitation Using an Improved Bulk Microphysics Scheme. Part II: Implementation of a New Snow Parameterization. *Monthly Weather Review*, *136*(12), 5095–5115. Retrieved from `http://dx.doi.org/10.1175/2008MWR2387.1` doi: 10.1175/2008MWR2387.1

Uliasz, M. (1994). Lagrangian particle dispersion modeling in mesoscale applications. In *Smr* (Vol. 760, p. 23).

Wang, J. W., Denning, A. S., Lu, L., Baker, I. T., Corbin, K. D., & Davis, K. J. (2007). Observations and simulations of synoptic, regional, and local variations in atmospheric CO¡inf¿2¡/inf¿. *Journal of Geophysical Research Atmospheres*, *112*(4). doi: 10.1029/2006JD007410

Xiao, J., Davis, K. J., Urban, N. M., & Keller, K. (2014, 6). Uncertainty in model parameters and regional carbon fluxes: A model-data fusion approach. *Agricultural and Forest Meteorology*, *189-190*, 175–186. Retrieved from `http://dx.doi.org/10.1016/j.agrformet.2014.01.022https://linkinghub.elsevier.com/retrieve/pii/S0168192314000318` doi: 10.1016/j.agrformet.2014.01.022